CHALMERS
UNIVERSITY OF TECHNOLOGY

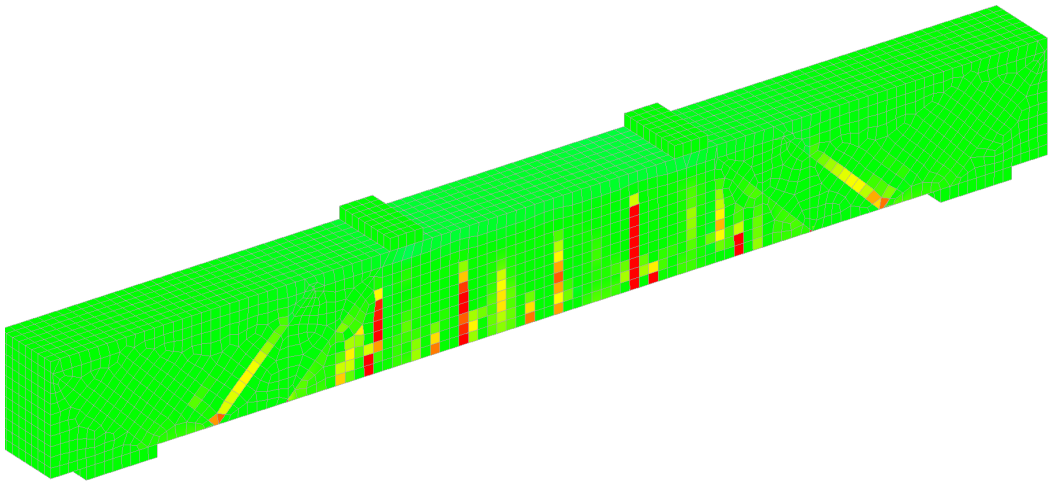

FE Analyses of Strengthened Concrete Beams with Corroded Reinforcement

Master's thesis in Master Program Structural Engineering and Building Technology

Carl Lindqvist Franklin
Milan Gotame

Department of Architecture and Civil Engineering
CHALMERS UNIVERSITY OF TECHNOLOGY
Master's thesis
Gothenburg, Sweden 2021

TO OUR PARENTS

Master's thesis

FE Analyses of Strengthened Concrete Beams with Corroded Reinforcement

Carl Lindqvist Franklin
Milan Gotame

Department of Architecture and Civil Engineering
Division of Structural Engineering
Concrete Structures Group
Chalmers University of Technology
Gothenburg, Sweden 2021

FE Analyses of Strengthened Concrete Beams with Corroded Reinforcement

Carl Lindqvist Franklin

Milan Gotame

Supervisor: Professor Karin Lundgren, Department of Architecture and Civil Engineering and Mattias Blomfors, Norconsult AB
Examiner: Professor Karin Lundgren, Department of Architecture and Civil Engineering

Department of Architecture and Civil Engineering
Division of Structural Engineering
Concrete Structures Research Group
Chalmers University of Technology
SE-412 96 Gothenburg, Sweden
Telephone +46 31 772 10 00

Cover: An illustration of strain output for a strengthened beam with meshing in four-point bending.

Department of Architecture and Civil Engineering
Gothenburg, Sweden 2021

FE Analyses of Strengthened Concrete Beams with Corroded Reinforcement
MILAN GOTAME
CARL LINDQVIST FRANKLIN
Department of Structural Engineering
Chalmers University of Technology

ABSTRACT

Existing concrete structures built between mid and late 1900s display increasing signs of deterioration due to adverse environmental conditions, reducing their load-carrying capacity. The existing structures are also required to carry increasing loads, which creates a need for increased capacity. For increased service life, existing deteriorated reinforced concrete (RC) structures need strengthening. The finite element method (FEM) has been proven as an efficient tool for numerical simulations to accurately predict the non-linear response of concrete structures. Fibre reinforced polymer (FRP) has successfully been used to strengthen sound structures, but its application on damaged concrete structures still needs to be investigated. This thesis presents non-linear finite element analyses to assess the flexural behaviour of corrosion damaged RC beams strengthened with externally bonded FRP. The modelling methods were validated against experimental results. Beams of four different categories were analysed: A reference beam, a corroded but non-strengthened beam, and corroded beams strengthened with GFRP and CFRP respectively. Furthermore, the strengthened beams were modelled with different modelling choices to investigate the effectiveness of FRP sheets and FRP U-jackets. Pre-loading and corrosion-induced cracks were incorporated by reducing the tensile strength of concrete elements at the location of cracks. Average and pitting corrosion were incorporated by reducing the cross-sectional area of the reinforcement corresponding to the measured corrosion. Interface elements were used to simulate the bond between FRP and concrete. The FE analyses were able to capture same failure modes as the tests. It was found that modelling of pitting corrosion was of major importance to depict a reliable load and deformation capacity of the beams. Sufficient yielding zone near the corrosion pit was required in the finite element modelling to avoid premature failure of the pitted rebars due to high strain localization. A combination of a FRP plate at the beam soffit with inclined U-jackets at the ends of the FRP plate provided sufficient flexural strengthening; thus, intermediate U-jackets were not necessary for the studied beam geometry and corrosion damages. However, with a GFRP sheet at the beam soffit, both inclined and intermediate U-jackets with sufficient interfacial stiffness were needed to provide full utilisation of the GFRP sheet for the studied beam geometry. To further study the effectiveness of the strengthening methods, it would be necessary to study beams with varying dimensions, corrosion patterns and levels, spacing and dimensions of FRP.

Keywords: Reinforced concrete structures, finite element analysis, corrosion, fibre reinforced polymer, CFRP, GFRP, strengthening, cracks, interface, U-jacket

What we do in life, echoes in eternity.
- Marcus Aurelius

Contents

PREFACE

This MSc thesis work was done in between January 2021 until June 2021 at the Division of Structural Engineering at Chalmers University of Technology, Sweden. The aim of this thesis was to do finite element analysis of strengthened concrete beams with corroded reinforcement and study the effectiveness of the strengthening methods.

We would like to express our heartily gratitude to our supervisor and examiner, Professor Karin Lundgren, for her huge support, excellent guidance and motivation throughout this research work. Prof. Lundgren has been a real source of energy and motivation for us. She is not only a great researcher with a brilliant mind set but she also cares about her students and loves to give constructive feedback to complete the research work with high quality. We have been inspired by her broad knowledge and friendly behaviour. We were able to gain useful knowledge and develop research potential while working with her. She always put us in priority and made it possible to solve the problems when we were stuck and feeling discouraged. Our grateful thanks also goes to our second supervisor Dr. Mattias Blomfors at Norconsult AB, for his valuable supervision, advice and feedback throughout the research work. It was not possible to complete this thesis work without his help and guidance.

This thesis was related to the experiments conducted by Jincheng Yang at the Division of Structural Engineering. We would like to thank Dr. Jincheng Yang for his valuable suggestions and help during the master thesis work. We wish him a successful career ahead and a bright future.

Swedish Institute had provided scholarship for Milan Gotame to pursue his Master's degree at Chalmers University of Technology. We send our acknowledgement to Swedish Institute for providing such a wonderful opportunity. We also would like to thank our all friends and present colleagues.

We would like to express our sincere gratitude to our lovely parents and siblings, for their continuous support, encouragement during all our years of study and life.

We have used Chalmers Centre for Computational Science and Engineering (C3SE) to run finite element analyses. We would like to acknowledge C3SE for providing their efficient services. Last but not the least, we would like to thank Chalmers University of Technology and the Division of Structural Engineering for providing a meaningful and exciting time during our master's study.

Life is a journey and we believe that the best is yet to come.

CARL LINDQVIST FRANKLIN
MILAN GOTAME
Gothenburg, June 2021

1 Introduction

1.1 Background

Concrete is a widely utilized material in structures for more than 150 years. This is because of its good fire performance, high stiffness, long life span, low maintenance, and cost [1]. Existing concrete structures built between mid and late 1900s display increasing signs of deterioration due to adverse environmental conditions resulting in a reduced capacity. The existing structures are also required to carry increasing loads, which creates a need for increased capacity. Variables such as higher volumes of commuter and cargo activity, heavier vehicles and earthquakes have increased the load on existing structures throughout the world [1]. To reduce the cost and environmental impacts due to new constructions, strengthening of structures such as bridges and buildings is of vital importance for both society and the environment.

The most common cause of degradation of reinforced concrete (RC) structures is chloride-induced corrosion [2]. Corrosion of reinforcement degrades concrete structures in several ways. Pitting corrosion causes local reduction of the cross-sectional area of the reinforcement, reducing the yielding and ultimate capacities but also the ductility [3, 4]. The increased volume of steel due to corrosion introduces splitting stresses resulting in spalling of the concrete cover and weakens the bond between the concrete and reinforcement [5]. The latter may cause anchorage failure and reduced load-carrying capacity.

Strengthening with fibre reinforced polymers (FRP) is a well accepted technique to increase the capacity of concrete structures [6]. There has been a large amount of research regarding strengthening of sound structures with FRPs [1], but its application on strengthening of corrosion-damaged structures is increasing in demand during recent years. Due to high strength to weight ratio and high modulus of elasticity, FRPs are easy to handle and effective for the improvement of structural behaviour [1]. Externally bonded FRPs to the soffit of a beam can increase the performance of the beam [7]; however, for heavily corroded RC structures, externally bonded FRPs can reduce the load capacity [8] and can not improve the stiffness and ductility capacity effectively [9, 10]. Triantafyllou and Al-Saidy [11, 9] suggested to do a patch repair of the damaged concrete cover before application of the FRP plates to improve the structural performance of the corrosion damaged RC structure. In spite of that recommendation, the high cost of a patch repair creates a demand for alternative strengthening techniques. It has been shown that the combination of transverse FRP wraps/U-jackets wrapped around the beam with FRP plates, can improve the flexural performance without a patch repair [9]. In damaged beams strengthened with vertical U-jackets, the failure modes were altered into FRP rupture or debonding instead of concrete cover spalling, optimizing the use of the FRP plates [12]. By replacing the vertical to 45 degree inclined U-jackets at the end of the FRP plates, the utilization of the plates could be improved further [12].

Nowadays, the finite element method (FEM) is commonly used for structural analysis of RC structures. Even though non-linear finite element analysis (NLFEA) requires high computational time and effort, it is an effective way to understand the physical behaviour and response of RC structures. Based on previous research [13, 14, 15, 16], FRP strengthened RC beams can be modelled and analysed accurately in FE software, thereby providing in-depth understanding of their non-linear structural behaviour. To analyse FRP strengthened beams with corroded reinforcement, it is necessary to validate the FE analyses to experimental results. In this master's thesis, FE models were developed in DIANA FEA 10.4 [17] and the analyses were validated to experiments carried out by Yang [18], consisting of four-point bending tests on sound, corrosion damaged but non-strengthened, and FRP strengthened RC beams.

1.2 Aim

The purpose of this master's thesis was to investigate promising strengthening techniques for corrosion damaged RC structures. More in detail, the aim was to study the effectiveness of the strengthening methods, regarding the load-carrying and deformation capacity in bending.

1.3 Objectives

Specific objectives pursued to reach the aim of the thesis were to:

- Validate FE modelling methods with experimental results.
- Investigate the structural effect of corrosion damage.
- Investigate different parameters of the strengthening methods to develop efficient strengthening solutions.

1.4 Limitations

The limitations of this project can be outlined as follows:

- The analyses focused on the flexural response.
- Strengthening of corrosion damaged RC beams were studied. Strengthening of slabs and columns were not considered.
- The FE analyses were validated by experiments with artificially induced corrosion, which structural effects could differ from natural corrosion.

1.5 Method

To achieve the goal of the thesis, a literature study was carried out to get a general understanding of the effects of corrosion on RC structures, strengthening of concrete structures, strengthening of corrosion damaged RC structures and finite element modelling of concrete structures. Thereafter, 3D FE models of a reference, corroded

and strengthened beams were developed and analysed in DIANA FEA. The analyses results were validated by comparison to the four-point bending tests of RC beams carried out by Yang [18]. The corrosion levels, material properties of concrete, reinforcement and FRPs were used according to measurements done by Yang. To study the effectiveness of the strengthening methods, different analyses were carried out in which the FRP components were applied in stages.

1.6 Outline of thesis

This thesis comprises eight chapters including an introductory part

In *Chapter 1* an overview of research background, aim, objectives, limitations and methods that were used to conduct the research work are presented.

Chapter 2 contains theoretical aspects and literature reviews related to effects of corrosion, strengthening methods for sound and corroded RC structures.

Chapter 3 presents theory behind Finite Element Analyses of RC structures.

Chapter 4 provides a brief overview of the experiments carried out by Yang [18].

Chapter 5 presents details regarding modelling of the reference, corroded and FRP strengthened RC beams. More in detail, the material properties of concrete, reinforcement, GFRP and CFRP, crack widths and corrosion levels used in the FE models are presented.

In *Chapter 6* the results from the FE analyses are presented. The results are compared and validated with the experimental results. The different failure modes, effects of corrosion, effects of externally bonded FRP and U-jackets on the flexural behaviour are also presented.

Chapter 7 discusses the results obtained from the FE analyses.

In *Chapter 8* conclusions are drawn based on the results and suggestions for future research are presented.

2 Strengthening of RC structures

2.1 FRP strengthening in general

There are many different strengthening methods that have been used traditionally for concrete structures. The more common ones have been to; i) increase the sectional area, ii) cast and install additional reinforcement bars, iii) post-stressing with tension rods, iv) or simply adding more supports. These methods have been working relatively well and will do so in the future. In the mid-70s, a method to install steel plates on the concrete surface was developed [19]. This method found fairly large use but has a number of issues: steel plates rust, they are heavy to install, joint plates are often needed and the installation to curved surfaces are complicated [19].

During recent decades, the development and use of advanced composite materials in structural engineering have increased. The reason for this increase is that extensive research and development have been carried out to produce clear guidelines for design and quality assurance. Furthermore, the insight in the industry of the benefits of using advanced composite materials has been steadily increasing. The most common and used name for advanced composite materials are fibre reinforced polymers (FRPs). The FRPs can consist of different materials, but the most common are glass fiber or carbon fiber (GFRP and CFRP respectively). Nowadays, these materials have been found to have major benefits in repair and strengthening of existing structures. FRPs are also used for new structures, where the FRPs are used as reinforcement and/or as prestressing of concrete structures [19].

What makes FRP materials distinctive is their high strength-to-weight ratio. The material can also easily be customized for many purposes. All of these reasons make FRPs suitable for strengthening where the use of many other materials are limited. The FRPs stress-strain relationship is considered to follow a linear elastic curve up until failure. Figure 2.1 shows the FRP stress-strain curve compared to the curve for steel. It is evident that the FRP lacks one of the major benefits of steel reinforcement, the plastic deformation capacity that provides a safety margin in the ultimate limit state of a structure.

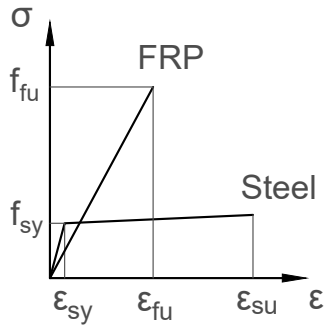

Figure 2.1: Comparison between the stress-strain for FRP and Steel.

Fibre reinforced polymers are, just like concrete, a type of composite material. The FRP is manufactured by continuous or short fibres which connect to each other by some type of polymer matrix. The matrix material is usually made from thermosets/resin, epoxy or vinylester. The fibre ratio in an FRP is 35-75% depending on the fibre material, manufacturing and desired properties. The remaining material is made of the polymer matrix. For strengthening of reinforced concrete structures, the most common FRP composition is carbon fibres with an epoxy matrix. Usually, FRPs are glued to the concrete surface, but there are examples of mechanical systems without glue as well. When the FRPs are glued to a concrete surface, it is common to use externally bonded FRP laminates. Before the laminates are glued to the surface, it is often recommended to use a primer on the surface to get good adhesion for the glue [19].

No complete design guidelines in the Eurocodes for strengthening with FRPs have been published yet. Instead, the current guidelines for design of strengthening of RC structures in Sweden are given in different textbooks. One of the more well-established and used textbooks in Sweden are "Kompositförsärkning av betong" [19]. In this textbook, a number of important design considerations are presented, such as design for bending and anchorage, design for shear etc. Specifically for bending, it is common to strengthen beams with externally bonded reinforcement (EBR) [19]. A principle of this strengthening technique is shown in Figure 2.2 where the glued FRP plate is presented as A_f.

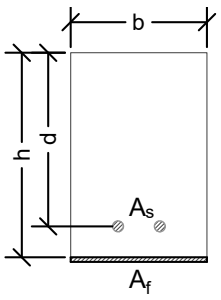

Figure 2.2: FRP strengthened concrete section with the EBR method.

A simplified estimation of the bending moment capacity for a given FRP area of the section seen in Figure 2.2 can be done according to Equation 2.1 [19], where f_y= yield strength of steel reinforcement, ε_{fu}= rupture strain of FRP and E_f= young modulus of elasticity for FRP.

$$M_d \approx 0.9(A_s f_y d + A_f \varepsilon_{fu} E_f h) \tag{2.1}$$

Alternatively, Equation 2.2 can be used to estimate the needed FRP sectional area for a desired bending moment capacity.

$$A_f \approx \frac{(M_d/0.9 - A_s f_y d)}{\varepsilon_{fu} E_f h} \tag{2.2}$$

These design estimations can be useful in early stages to estimate material needed and the cost of strengthening. However, for later stages more detailed calculations of other sections might need to be analysed.

Sufficient anchorage of the FRPs is essential to get full utilization of the strengthening. The anchorage is usually governed by the quality of the concrete, provided that the glue has been applied properly. Specifically for strengthening with FRPs, the normal and shear stresses arising at the end of the FRPs need to be analysed. A common way to increase the anchorage capacity of the bonded FRP is to wrap and glue transverse FRPs vertically around the end of the EBR FRP; this method is also called U-jackets. The U-jackets are even more effective if they are glued in a 45 degree angle towards the support, perpendicular to possible shear cracks [19]. The principle of the U-jackets can be seen in Figure 2.3.

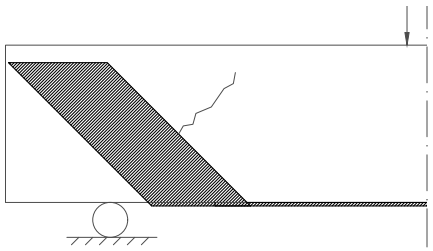

Figure 2.3: Inclined U-jacket towards the support.

2.2 Failure modes

As shown in Figure 2.4, Pham [20] stated different failure modes of a strengthened concrete beam in flexure as: 1) Concrete crushing, 2) FRP rupture, 3) Shear failure, 4) Concrete cover separation, 5) Plate end interfacial debonding, 6) Intermediate flexural debonding (IC debonding), 7) Shear-induced debonding, also known as critical diagonal crack (CDC) debonding). Modes 4 to 7 are premature debonding failure, in which modes 4 and 5 are initiated at or near the plate end, while modes 6 and 7 are initiated at intermediate sections.

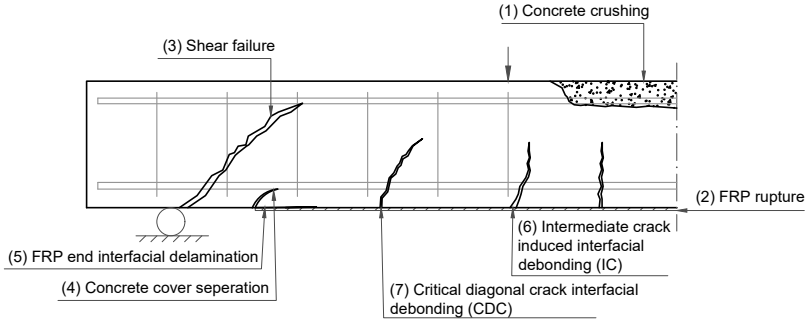

Figure 2.4: Failure modes of FRP strengthened concrete beam, redrawn from [20].

2.2.1 Concrete crushing

The failure modes of a non-strengthened and undamaged reinforced concrete beam are highly dependent on the reinforcement ratio. With a low amount of tensile reinforcement, the beam is expected to fail in bending with yielding and subsequent concrete crushing, or possibly rupture of the reinforcement bars. With a high amount of reinforcement, the beam is expected to fail by concrete crushing without reinforcement yielding [21]. More in detail, it is desirable to avoid concrete crushing before yielding of the reinforcement, to avoid the brittle failure of early concrete crushing.

2.2.2 FRP rupture

If the rupture strain of the FRP sheets is reached before the crushing of concrete but after the yielding of the tensile reinforcement, the failure mode will be governed by the FRP rupture [22].

2.2.3 Intermediate crack-induced debonding

Intermediate crack-induced debonding, commonly known as IC debonding, of FRPs can be caused by the relatively large interfacial stresses between the concrete and FRP generated due to the opening of flexural or shear cracks at the tensile side of the beam. When the failure is developed due to shear cracks, it is known as critical diagonal crack (CDC) interfacial debonding. As soon as the interfacial stresses exceeds the bond strength between the concrete and FRP, debonding of the FRP begins at the position of cracks and extends towards the closest sheet end. The IC debonding can be controlled by reducing the maximum strain allowed in the FRPs at the tensile side [22]. Debonding due to CDC has been found to be the most critical due to the brittleness of its failure [20].

2.2.4 End debonding

Debonding of the FRP plate end from the concrete beam can take place in two ways: either by end interfacial delamination failure or by concrete cover separation. They are both related to high shear stresses between the concrete and the end of the FRP plate. Though, it has been reported more common with concrete cover separation [22]. Concrete cover separation is initiated by high shear and normal stresses at the end of the FRP plate. This creates peeling stresses on the concrete, which might result in separation of the concrete cover if there is high risk of shear cracks, see Figure 2.5. However, when the shear capacity is high enough, high interfacial stresses at the connection between the concrete and FRP sheets/plates may result in interfacial separation. This separation begins between the FRP plates and the adhesives, or the adhesives and the concrete, depending on which interface is weaker.

Figure 2.5: Concrete cover separation of FRP strengthened beam, permission from [22].

2.3 Structural effects of corrosion

2.3.1 Mechanism of corrosion

Among many factors, chloride-induced corrosion of reinforcement affects the capacity of RC structures. In sound structures, the alkaline environment created during hydration of concrete protects the reinforcement by forming a passive layer. However, this passive protective layer can be damaged by chlorides or carbonation, which enables reinforcement corrosion. Corrosion has adverse effects on reinforcement and concrete. Corrosion reduces the cross-sectional area of the reinforcement bars [23, 24], and the rust produced occupies a larger volume than the original reinforcement. The increased volume thereby produces splitting stresses to surrounding concrete which ultimately leads to cracking and spalling of concrete. The corrosion-induced cracks further trigger the corrosion rate. Cracking and spalling of the concrete cover reduces bond capacity [25]. According to CEB-fib [26], corrosion of reinforcement can be categorized into general and local corrosion. The general corrosion is due to uniform corrosion of rebar, whereas pits are formed due to local corrosion. The overall aspects of corrosion mechanism and its structural consequences have been studied by Cairns et al., see Figure 2.6 [27].

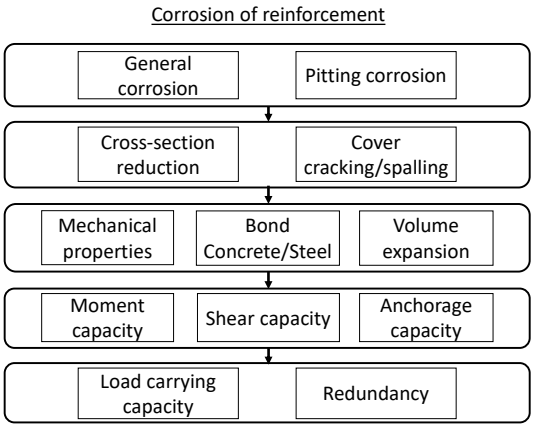

Figure 2.6: Effects of corrosion on structural behaviour of a concrete. Reproduced from Cairns et al. [27].

2.3.2 Mechanical properties of corroded reinforcement

Researchers such as Zhang et al., Apostolopoulos et al. and Fernandez et al. [28, 3, 29] have found that corrosion has adverse effects on the mechanical properties of reinforcement, such as strength, deformation capacity and modulus of elasticity. Large localized strains are generated due to pitting corrosion; since the cross-sectional area is substantially smaller at the pits, high stress concentration and large strains are generated compared to the other sections of the reinforcement bar, see Figure 2.7 [4]. Furthermore, because the length of the local pit is short, the strain at the pit is larger than the average strain over the entire length of the reinforcement bar [30]. Due to the localized large strain, the deformation capacity of the reinforcement is reduced, thereby causing brittle failure of structures [24]. It has been found that for high corrosion levels, yield penetration will not spread outside of the pitted zone if the local corrosion exceeds a critical corrosion level [4]. The critical local corrosion level was found to be $1 - f_y/f_u$, where f_y and f_u are yield strength and ultimate strength respectively.

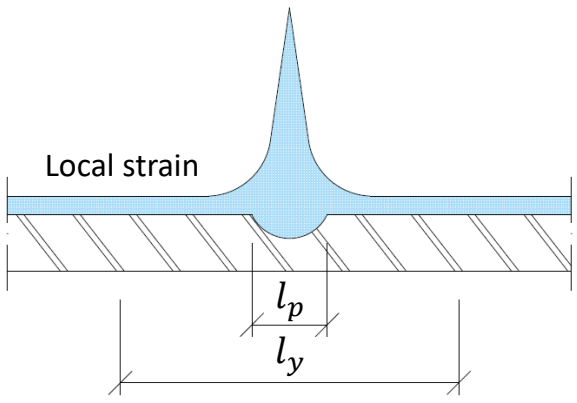

Figure 2.7: Diagram showing high local strain at pit with pit of length (l_p) and yield length (l_y) reproduced from [4].

2.3.3 Bond between concrete and corroded reinforcement

The bond stress between the concrete and reinforcement is the major path to transfer load in reinforced concrete structures. Friction, chemical adhesion and mechanical interaction between concrete and steel are the main components that govern the bond. The chemical bond is quite weak and is prone to break at low stresses. The volume expansion of corrosion introduces splitting stresses on the concrete, which leads to cracking and reduction of the bond.

2.3.4 Mechanical behaviour of corrosion damaged RC structures

Corrosion influences several aspects of the structural behaviour of RC structures, for example stiffness, load-carrying capacity and deformation capacity, see Figure 2.6. The shear and moment capacities of the structures are decreased due to pitting corrosion of the reinforcement bars. The brittle behaviour of corroded rebars changes the force and moment redistribution, reducing the load-carrying capacity and seismic resistance as well. The spalling of concrete cover decreases the cross-section and internal lever arm, thereby reducing the flexural capacity. Moreover, the reduced bond between the surrounding concrete and corroded reinforcement may lead to anchorage failure and reduced shear capacity of the structure. Furthermore, the cracks formed due to corrosion increases the chance of more enhanced chloride ingress and accelerated corrosion.

2.4 Strengthening of corrosion damaged RC structures

Since 1980s, researchers have focused on strengthening of RC structures using externally bonded FRP. It is common to use EBR FRP on the tension side of the RC member. This method of strengthening has been found effective to increase the flexural capacity; i.e to increase the load-carrying capacity and service life of structures [9, 31, 32, 33]. EBR FRP strengthening have been successfully implemented for sound concrete structures. However, its' application on corrosion damaged RC structures is still of research interest. In this chapter a synthesis of various research results are presented [34, 32, 35, 36, 37, 11].

There are mainly two ways to strengthen a corrosion damaged RC structure: with or without patch repair. The load-carrying capacity of concrete beams with different degree of damages can be increased satisfactorily by a patch repair of the damaged concrete cover, but the effectiveness of the patch repair decreases with increased corrosion level [37, 34, 11]. As described by Linwang and Triantafyllou, to increase the load bearing capacity of beams with high corrosion levels, it was necessary to replace the damaged concrete cover by a new polymer mortar layer before FRP application [37, 11]. A good bond condition had to be achieved between the new and old concrete [11]. However, the results were similar when U-jackets were applied

without doing a patch repair [9]. It was concluded that U-jackets were effective to increase the capacity of highly corroded beams, but the layout of U-jackets was important to obtain good results [38]. Furthermore, it was found that two layers of FRP sheets on the beam soffit in combination with U-jackets increased the stiffness of a corroded beam. However, it exhibited a more brittle behaviour than a beam with a continuous FRP sheet wrapped up 65 mm on each side of the beam. It was concluded that the layout of the FRP strengthening affects the behaviour, even though the amount of FRP used for strengthening is the same [38].

Fu et al. and Triantafyllou have studied the effectiveness of U-jackets at the end of FRP plate to mitigate concrete cover separation [39, 11, 12]. It was concluded that a certain minimum thickness of U-jacket was necessary to completely mitigate the concrete cover separation due to corrosion [39, 11]. Even though two layers of U-jackets did not show any difference in load capacity, the ductility behaviour was better than one layer of U-jackets at the FRP sheet end. Furthermore, with inclined U-jackets at the end of the FRP sheet, the ultimate load and ductility was successfully increased even further [39]. Thus, 45 degree inclined U-jackets could increase the efficiency of the FRP sheets due to tensile force transfer mechanism from FRP plate at beam soffit. The ultimate load capacity, ductility and utilisation of the FRP sheet were increased significantly due to the application of 45 degree inclined U-jackets by changing the failure mode from IC debonding to concrete crushing or rupture of FRP sheet [12]. In general, the 45 degree inclined U-jackets would be activated due to debonding of the FRP plate. Even after the complete debonding of the soffit plate, 45 degree inclined U-jackets were able to hold the debonded FRP sheets in the beam soffit in position and transfer the strain generated in between the concrete and FRP sheets effectively to the inclined U-jackets [12].

It has also been found that intermediate U-jackets were effective to increase the capacity of highly corroded beams [11]. In practical application, the amount of FRP needed for strengthening is vital due to its relatively high cost. It has been found that high amounts of FRP does not necessarily improve the capacity of damaged concrete structures effectively [39]. Thus, it is worthwhile to do a parametric study of different FRP layouts and dimensions to get an economic, efficient and reliable strengthening method.

3 FEA of concrete structures in general

Previously, two dimensional (2D) and three dimensional (3D) FE modelling have been used to analyse sound, corroded and strengthened concrete beams [40, 41, 42, 43, 44]. Even though 2D symmetrical FE modelling can lead to good results [40, 41], 3D FE modelling may be needed for reasons such as: i) The potential corrosion effects are typically 3D in nature ii) For a particular beam size, the assumption of plane stress or plane strain may not be completely true and iii) The FRP strengthening is not applied to the entire width of the beam. The reinforcement can be modelled by truss, beam and 3D continuum elements [44]. The continuum elements for reinforcement can in many cases be unnecessarily detailed. It has been found that modelling the reinforcement using beam element exhibits good agreement with experiments and can be computationally efficient [43].

To get accurate results from finite element analysis (FEA), the non-linear material properties of concrete and reinforcement need to be taken in account [40]. The non-linear FEA (NLFEA) results of reinforced concrete structures is governed mainly by [45]: i) Material non-linearity of concrete in both tension and compression with strain localization, and of steel with yielding and hardening, ii) Bond stress-slip relationship between concrete and reinforcement, iii) Convergence issues mainly after the cracking of concrete, iv) Load application and boundary conditions. The non-linear concrete properties in tension and compression can be represented by different non-linear models such as Hordijk and exponential tensile curve or parabolic, multi-linear and Thorenfeldt for the compression curve. The non-linear material behaviour of reinforcement can be modelled by stress-strain relationship which should be able to describe the yielding, hardening and rupture. The interaction between concrete and reinforcement is commonly incorporated in two different ways: i) by assuming perfect bond, i.e concrete and steel have the same strain; or ii) by applying a bond stress-slip relationship between concrete and reinforcement; this gives a more realistic behaviour in terms of crack patters and anchorage capacity. A bond stress-slip relationship between concrete and reinforcement is given in Model Code 2010 [26].

Normally, cracking of concrete can be modelled by a discrete-crack or smeared-crack approach. In the earlier one, the geometrical cracks are treated as displacement discontinuities. The tensile fracture zone is defined before the meshing of a FE model in the discrete-crack approach, which makes it more complicated and unpractical. To overcome this issue, the smeared crack approach, which considers the crack in a continuous geometry, can be used. Two commonly used models exist: the fixed crack model and the rotating crack model. In the rotating crack model, a crack will reorient with the loading or material response, and the orientation of the crack is considered perpendicular to the principal tensile stress [46, 47, 45]. Whereas in the fixed crack model, the direction of a crack will remain unchanged after initiation.

This creates shear stresses that are built up due the rotating principle stresses after crack initiation [45]. Moreover, the tension-stiffening effect, i.e the increased stiffness due to uncracked concrete in-between the cracks, will also be automatically considered in FE analysis including bond-slip relation between concrete and reinforcement [45]. It is important to study the crack development and concrete crushing to build a good basis for the modelling of FRP strengthened beams [41].

As pitting corrosion, also called local corrosion, has a major impact on the reduction of ultimate capacity and ductility of a beam, inclusion of local corrosion in the FE model is of high importance to predict the capacity of corrosion damaged RC structures. It has been shown that reduction of cross-sectional area of longitudinal reinforcements at the location of pitting and general corrosion is able to represent the reality [48]. According to Blomfors, weakening of concrete elements at the location of bending cracks and corrosion-induced cracks in a FEA model gives reasonable results in comparison to test results in terms of load vs deflection and ultimate capacity [49, 44].

Normally, FRP strengthening is modelled in two different ways in a 3D model, i) As shell elements with an orthotropic material; ii) As brick elements defined with an isotropic 3D material representing the adhesive and unidirectional and bi-directional smeared reinforcement of fibres [13]. In the case of a 2D model, 1D beam elements with an isotropic material can be used [50, 15]. The bond behaviour between the concrete and FRP has an influence on debonding of FRP and stiffness of strengthened RC structures. Researchers have used different methods to model the interface properties between concrete and FRP in non-linear FEA. According to current literature, two different methods have been found more common: i)Perfect bond in between concrete and FRP [51]; ii) Interface elements between the concrete and FRP [16, 52]. Among these two methods, the interface elements have been used most commonly to simulate the interaction between concrete and FRP. In this method, the interfacial properties can be assigned by defining the constitutive bond stress - slip relationship or shear traction-separation law [53, 54]. The bond stress - slip relationship commonly used comprises of two phases: i) The first elastic phase, the bond stress increases with slip until the bond strength of the interface reaches its maximum strength; ii) In next phase, the bond stress decreases with increased slip [55].

4 Summary of experiments

The RC beams analysed in this FEA study were tested in four-point bending until failure by Yang [18]. The first test group, RN, included two sound beams to act as reference. Among the deteriorated beams, two were non-strengthened (DN), three were strengthened with GFRP (DG) and three were strengthened with CFRP (DC), see Table 4.2. In the following sections, the geometry, corrosion levels, and other material properties from the experimental study are presented. For more detailed information about the tests, the reader is referred to Yang [18].

4.1 Beam geometry and material properties

The tested RC beam specimens have 2.1 m length, 225 mm height and 150 mm width as shown in Figure 4.1. The concrete mix had proportion of cement:sand:gravel:water = 1:2.46:1.90:0.43 by weight. Concrete cubes (side length 150mm) have been used in standard compressive tests to obtain the compressive strength of concrete, and cylindrical specimens (100mm diameter and 200mm height) have been used to obtain the elastic modulus [18]. Wedge-splitting tests have been carried out to obtain tensile fracture energy of concrete. The stress versus strain relationship and young modulus of the reinforcement bars has been measured by standard tensile tests [18]. The properties of concrete and reinforcement at the time of structural failure tests are presented in section 5.3 and 5.4 respectively. The longitudinal reinforcements had a diameter of 12mm and 10mm, see Figure 4.1(right). The level of tensile and compressive rebars from bottom surface of beam for the different beam categories are shown in Table 4.1. The stirrups of diameter 8mm were spaced equally at distance of 125mm at outer 750mm region with a clear cover of 20mm as shown in Figure 4.1.

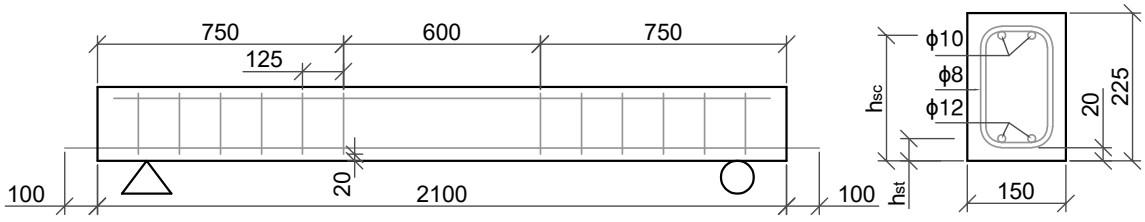

Figure 4.1: Beam geometry and cross-section [18].

Table 4.1: Position of the tensile and compressive steel reinforcement bars in beam specimens in relation to the beam soffit [18].

Specimens	h_{st} [1][mm]	h_{sc}[1][mm]
RN1	41	190
RN2	40	189
DN1	40	191
DN2	N.A.	N.A.
DG1	39	189
DG2	39	190
DG3	38	190
DC1	38	189
DC2	39	191
DC3	41	192

[1] h_{st} - Level of bottom rebars
[2] h_{sc} - Level of top rebars

4.2 Pre-cracking and accelerated corrosion

To achieve a realistic corrosion pattern with both general and pitting corrosion in the deteriorated beams, they have been pre-cracked by three-point bending followed by accelerated corrosion of the tensile reinforcement bars at mid 600mm zone. The three-point bending and the accelerated corrosion resulted into transverse bending cracks and longitudinal corrosion-induced cracks. The magnitude and location of these pre-cracks are presented in Appendix B.

4.3 FRP strengthening method

The six beams in groups DG and DC have been strengthened after the accelerated corrosion stage. Figure 4.2 shows how the FRPs have been bonded externally to the concrete surface. For group DG, a 1500 mm long and 150 mm wide GFRP laminate was attached to the beam soffit. For the DC group, a 1500 mm long CFRP plate with a cross section of 100x1.45 mm^2 has been attached to the beam soffit. After 48-hours of curing, U-jackets made of CFRP have been installed to the DG and DC beams, see Figure 4.2. The fibers of the U-jackets were oriented in the transverse direction. Vertical U-jackets had one layer of CFRP fabric, whereas the 45° inclined U-jackets had three layers of CFRP fabric. After bonding of the FRPs, the beams have been cured for four weeks prior to the four-point bending tests.

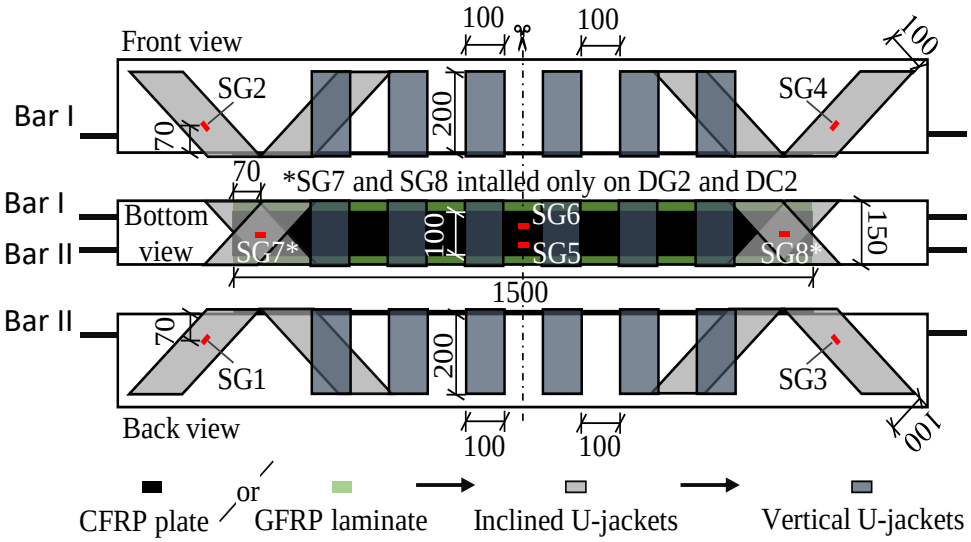

Figure 4.2: FRP strengthening method used by Yang to the corrosion damaged concrete beams [18].

4.4 Four-point bending test

The beams with an effective span of 1.8m have been tested in four-point bending as presented in Figure 4.3. Variable differential transformers (LVDT) have been used to measure the net deflection at the middle of beam and at the two steel supports. In the FRP composites, the axial strains at critical positions have been measured by strain gauges (SG1-SG8), see Figure 4.2.

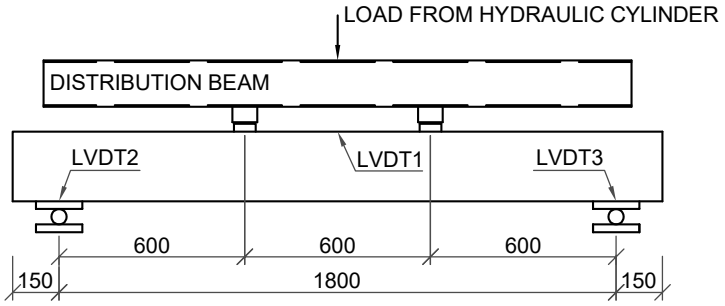

Figure 4.3: RC beam subjected to four-point bending until failure [18].

4.5 Corrosion levels

After the four-point bending tests, the tensile reinforcement bars have been extracted from the beams and the corrosion levels have been measured using 3D optical scanning [18]. The measured cross-sectional area of the rebars before and after corrosion are presented in Appendix C. Information about the average and pitting corrosion levels are shown in Table 4.2.

Table 4.2: Corrosion levels in tensile reinforcement bars tested by Yang, I and II represent numbering for the bars [18].

Specimen	Flexural strengthening material	Average corrosion level [%]		Max. local corrosion level [%]	
		I	II	I	II
RN1	-	-	-	-	-
RN2	-	-	-	-	-
DN1	-	20	19	50	48
DN2	-	20	21	46	54
DG1	GFRP	22	17	51	40
DG2	GFRP	21	20	43	54
DG3	GFRP	18	23	43	53
DC1	CFRP	23	20	53	55
DC2	CFRP	21	22	49	41
DC3	CFRP	21	22	54	57

5 NLFEA of experiments

The flexural behaviour of reference, corrosion damaged and FRP strengthened RC beams tested by Yang [18] was studied with 3D NLFEA in DIANA FEA [17]. The concrete beams were modelled using 3D solid (continuum) elements and the tensile reinforcements were modelled as beam elements. The interaction between the bottom longitudinal reinforcement, FRPs and concrete was modelled with interface elements. The top reinforcement and the stirrups were modelled as embedded reinforcement with full interaction. In this chapter, the FE modelling approaches are presented.

5.1 Overview of FE-models

Out of ten tested specimens, see section 4.5, one beam from each of the four different categories were modelled in DIANA 10.4. Reference beam (RN1), corroded but non-strengthened specimen (DN1) and corroded beams strengthened with GFRP and CFRP (DG1 and DC1 respectively) were modelled with different modelling choices. An overview of the analyses with different modelling choices is presented in Table 5.1.

Table 5.1: Overview of FE models

Beam	FEA model	Description
RN1	RN1_FEA	Reference RC beam
DN1	DN1_FEA	Three major corrosion pits in each rebar
	DN1P1_FEA	One major corrosion pit in each rebar
	DN1P1E_FEA	One major corrosion pit in each rebar with extended yield penetration length
DG1	DG1N_FEA	Corroded but non-strengthened
	DG1S_FEA	Corroded, strengthened with GFRP sheet only
	DG1IU_FEA	Corroded, strengthened with GFRP sheet and inclined U-jackets
	DG1NLI_FEA	Corroded, strengthened with GFRP sheet, vertical and inclined U-jackets, non-linear interface for U-jackets
	DG1_FEA	Corroded, strengthened with GFRP sheet, vertical and inclined U-jackets, linear interface for U-jackets
DC1	DC1N_FEA	Corroded, but non-strengthened
	DC1P_FEA	Corroded, strengthened with CFRP plate only
	DC1IU_FEA	Corroded, strengthened with CFRP plate and inclined U-jackets
	DC1_FEA	Corroded, strengthened with CFRP plate, vertical and inclined U-jackets

5.2 Idealisation of a beam

Since the corrosion damage was not symmetrical for the damaged RC beams, the 3D models of RN, DN, DG and DC beams were modelled with their complete geometry. The reference beam was used as a base, and was further developed for modelling of the corroded and strengthened beams. The concrete was modelled with 3D continuum elements. The idealisation of the reference beam for the 3D FE modelling can be seen in Figures 5.1, 5.2, and 5.3. The tensile longitudinal reinforcement bars were modelled as one-dimensional beam elements while the top rebars and stirrups were assigned as embedded reinforcement. Moreover, the tensile rebars were connected to surrounding concrete by interface properties as described in section 5.6. In the experiments, roller supports and steel plates were used at the supports and steel plates at the loading points. In the FE model, the loading and support plates were modelled as 25 mm thick plates with solid elements, and thin wooden plates were applied under them to avoid stress concentration on the concrete elements near the plates. The centre nodes along the support plates were restricted to displace vertically at both left and right support plates, and restricted horizontally at one of the supports, see Figures 5.1 and 5.2. The support and loading plates were connected to the concrete surface with structural plane interface elements. The load distribution beam, used in the tests, was idealized with beam elements. The end nodes of the loading beam were tied to the center lines of the load plates in their vertical displacement. Furthermore, the center node of the loading beam was restricted to displace horizontally to ensure the stability of the loading beam. The deformation controlled load was applied through the centre of the loading beam, see Figures 5.1 and 5.2. The rebar numbering which is used for corrosion modelling is presented in Figure 5.3.

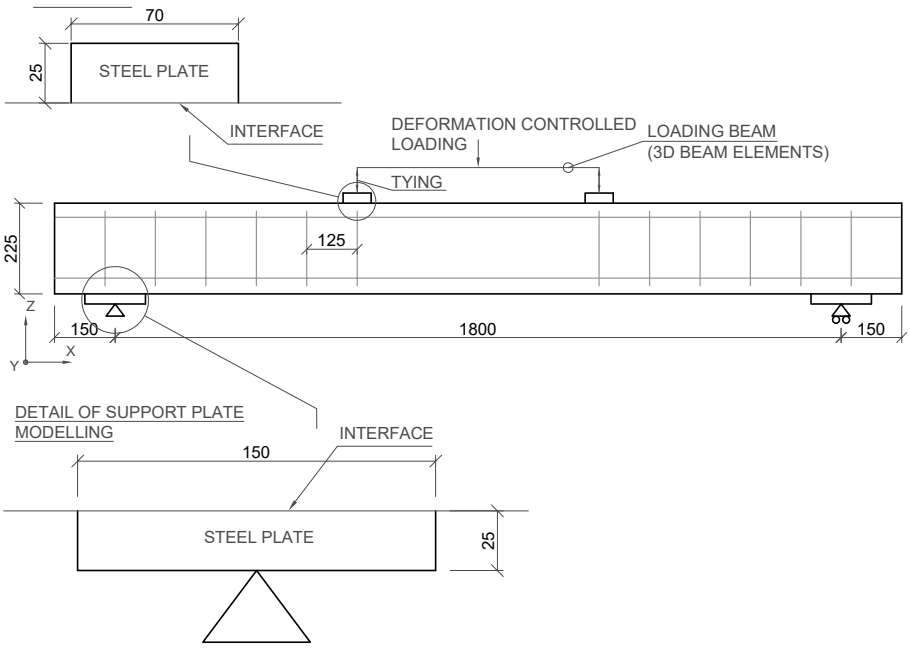

Figure 5.1: Idealisation of the reference beam.

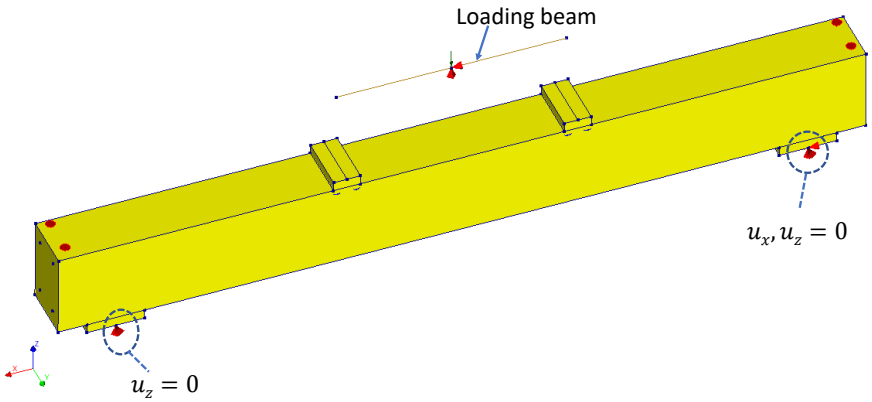

Figure 5.2: 3D view of the idealised reference beam.

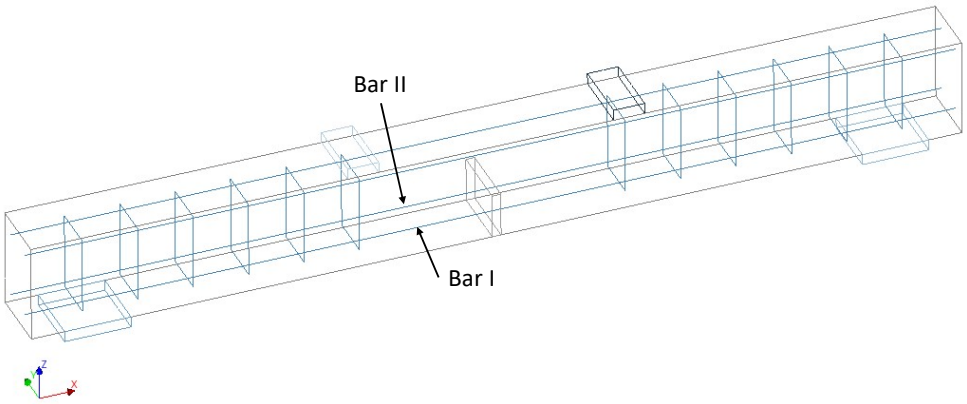

Figure 5.3: 3D view presenting the rebar numbering.

5.3 Material model for concrete

In Table 5.2, the material properties of concrete used in the FEA are shown; these are based on compression and wedge split tests conducted by Yang [18]. Cracking of concrete was modelled by smeared rotating crack model based on total strain in DIANA 10.4. The crack band width was assumed as $\sqrt[3]{V}$, where V is the volume of a 3D concrete element, as proposed by Rots [56]. This crack band width was later verified against approximate length of zones with localised strains in the analysis. For the reference beam, the tensile strength of the concrete elements at the mid section, see Figure 5.7, was reduced by 20% to promote the strain localization; this largely improved the convergence.

Table 5.2: Material properties of concrete used in the non-linear analyses.

Concrete properties	**Value**	**Reference**
Mean compressive strength [MPa] $f_{cm} = 0.8f_{cm.cube}$	63	[18, 26]
Mean tensile strength [MPa] $f_{ct} = 2.12ln(1 + 0.1f_{cm})$	4.21	[26]
Young's modulus [GPa] E_{cm}	33.3	[18]
Tensile Fracture Energy [N/m] G_F	134	[18]
Compressive Fracture Energy [N/m] $G_C = 250G_F$	33500	[26]

The tensile behaviour of concrete was characterized by the tensile strength-strain relationship introduced by Hordijk [57], as shown in Figure 5.4 (a). The behaviour of concrete in compression was taken into account by a parabolic compression curve according to Feenstra [58], with a softening branch as shown in Figure 5.4 (b), which is characterized by Equation 5.1:

$$\begin{aligned} \alpha_{c/3} &= \frac{-1}{3}\frac{f_{cm}}{E_{cm}} \\ \alpha_c &= 5\alpha_{c/3} \\ \alpha_u &= \alpha_c - \frac{3}{2}\frac{G_c}{hf_{cm}} \end{aligned} \tag{5.1}$$

The softening branch of the compression curve is based on the compressive fracture energy. A reduction factor of 0.6 due to lateral cracking was used according to Vecchio & Collins [59].

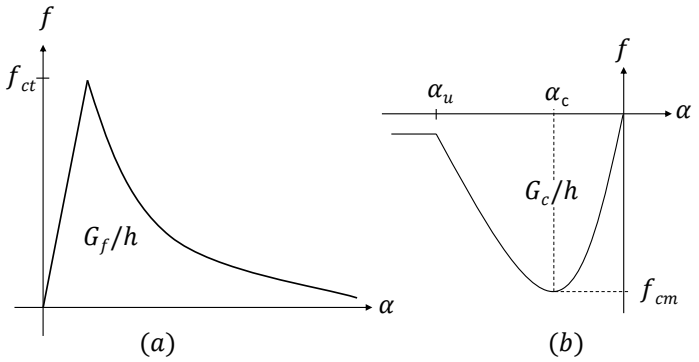

Figure 5.4: (a) Tensile stress-strain curve proposed by Hordijk [57] (b) Parabolic compression curve proposed by Feenstra [58], here α and h represents strain and crack band width, respectively.

5.4 Material model for reinforcement bars

The tensile stress-strain curve as shown in Figure 5.5 was given as an input to simulate the behaviour of reinforcement in the FE analysis. The stress-strain properties of the steel reinforcement bars were obtained from standard tensile tests performed by Yang [18]. As shown in Figure 5.5, six tensile tests of both the top and bottom

rebars have been carried out. A curve fitting the average of the test results was used as input in the FE analyses. The material parameters of tensile, compression reinforcement and stirrups are presented in Appendix A.

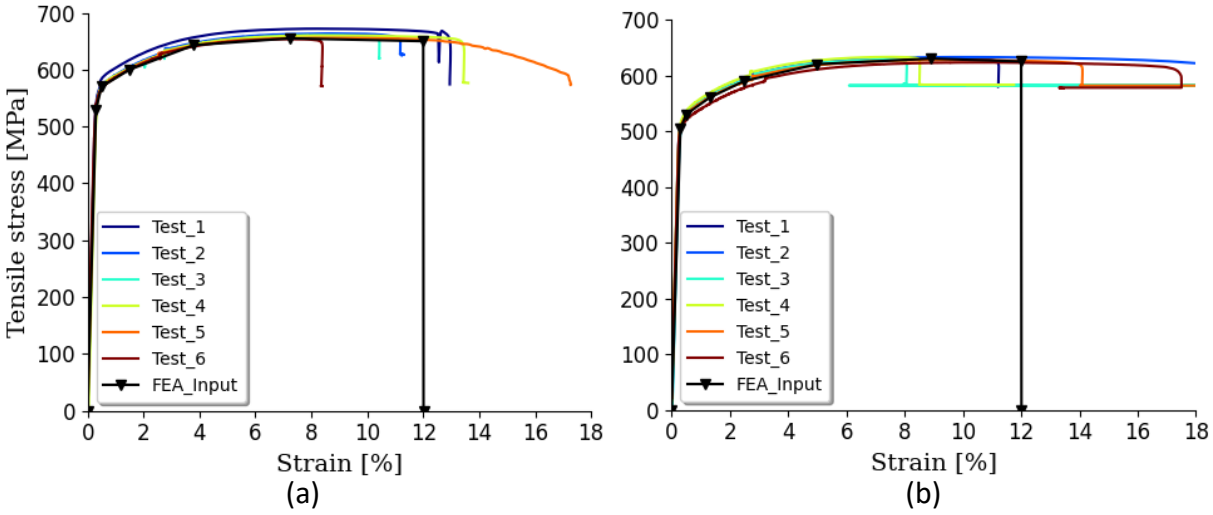

Figure 5.5: Tensile stress-strain relationship of longitudinal reinforcements from tensile test and indicating how it was implemented in FE modelling for: (a) bottom rebars (b) top rebars.

5.5 Loading and support plates

Steel plates were used at the position of support and loading points to avoid high stress concentration. Linear properties of the steel plates were assumed with an E-modulus of 200 GPa and a Poisson's ratio of 0.3. Interface properties were assigned between concrete and steel plates according to Belletti [40], see Table 5.3. Here, DSSX, DSSY are shear stiffness modulus along x and y-directions respectively and DSNZ is normal stiffness modulus along z-direction.

Table 5.3: Steel plate-concrete interface properties [40].

$DSNZ[N/m^3]$	$DSSX[N/m^3]$	$DSSY[N/m^3]$
$3.42 \cdot 10^{13}$	$3.42 \cdot 10^{5}$	$3.42 \cdot 10^{5}$

5.6 Concrete-reinforcement interaction

To predict better crack patterns and proper flexural response of the beam beyond cracking, the interaction between concrete and main reinforcement was modelled with a bond stress-slip relationship according to *fib* Model Code 2010 [26]. The "Good" bond condition and "Pull-Out" failure condition was assumed in *fib* Model Code bond slip formulation. As shown in Figure 5.6, the Model Code bond-slip relation was characterized by $\tau_{bmax} = 19.84$ MPa, $\tau_{bf} = 0.4\tau_{bmax}$, $s_1 = 1$ mm, $s_2 = 2$ mm and $s_3 = 5$ mm. The shear stiffness of concrete-reinforcement interface was set to be 10^{12} N/m^3; this value is however overruled by the nonlinear bond stress-slip

relationship. The normal stiffness was 10^{13} N/m^3. Between top reinforcement and concrete, as well as between stirrups and concrete, full interaction was assumed.

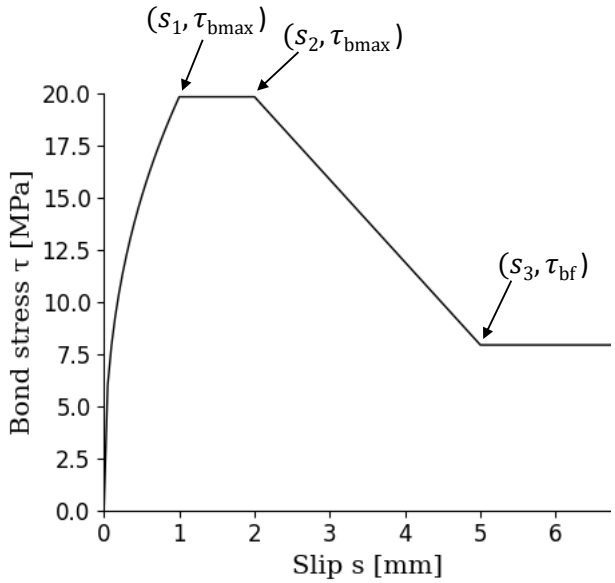

Figure 5.6: Bond stress-slip relationship between tensile reinforcement and concrete, according to Model Code 2010 [26].

5.7 FE mesh

The concrete was modelled with 3D solid continuum elements of brick, tetrahedron, pyramid, and wedges (HX24L, TE12L, PY15L, TP18L, respectively), all with linear interpolation and gauss integration. The average size of element lengths was set to 20 mm; lower than minimum of $(\frac{l}{50}, \frac{h}{6}, \frac{b}{6})$, as suggested by Hendriks [60]. A 3D view of a meshed beam can be seen in Figure 5.7. The interface between the concrete beam and steel plates was modelled using Q24IF elements. Longitudinal reinforcement bars were modelled as beam elements. The loading beam was modelled with three-dimensional two nodal beam elements (L12BEA).

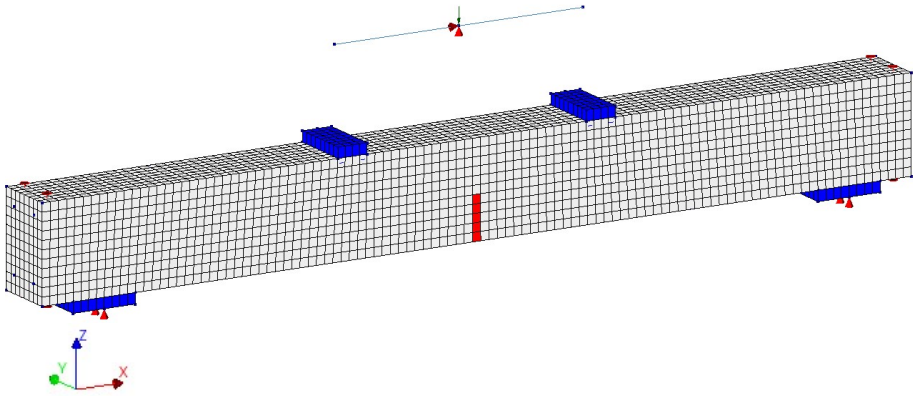

Figure 5.7: 3D FE mesh of the reference beam (FE model RN1). Grey color indicates concrete, red color shows weakened concrete elements, and blue color represents loading and support plates.

5.8 Incorporation of pre-existing cracks

For beams in the categories DN1, DG1 and DC1, the cracks induced due to pre-loading (transverse cracks) and corrosion (longitudinal cracks) were incorporated by reducing tensile strength for the corresponding concrete elements, as suggested by Blomfors et. al. [49, 44]. The reduced tensile properties of the weakened concrete elements were determined from a bilinear mode-I stress-to-crack width relationship with a break point according to Wittmann et al, see Figure 5.8(a) [61].

$$\sigma_s = 0.25 f_{ctm}; \quad w_{ult} = \frac{5G_f}{f_{ctm}} \quad [26]; \quad w_s = 0.15 w_{ult} \tag{5.2}$$

Here, $\sigma_s = 1.05$ MPa, $w_{ult} = 0.159$ mm, $w_s = 0.0239$ mm.

The transverse and longitudinal cracks, which have unique crack widths, were extracted from the test results [18]. The cracks which were measured on the tensile edge of the beam were considered in FE modelling. For each of the transverse cracks, the crack width was assumed to be constant along the width of beam. Moreover, the longitudinal cracks were assumed to have same crack width through out their crack length. For the crack widths larger than the breaking point in the bilinear mode-I stress-to-crack width curve, the widest crack width was chosen. Furthermore, for the cracks with a width close to or larger than the ultimate crack width (w_{ult}), tensile strength corresponding to $0.99 w_{ult}$ was assumed.

For chosen crack width, the tensile stress ($f_{ct,c}$) and residual fracture energy, ($G_{F,wc}$) were determined from the bilinear mode-I stress-to-crack width curve, Figure 5.8(a). The stress-crack width relationship was then converted to the corresponding stress-strain relationship by dividing with E_{cm} and the crack band width (h) respectively, see Figure 5.8(b) and (c). The ultimate strain ($\varepsilon_{wc,ult}$), in resulting stress-strain relationship, for the weakened elements were calculated so that residual fracture

energy, ($G_{F,wc}$) divided by the crack band width, is equal to the area under the stress-strain curve, in Figure 5.8(c).

$$\varepsilon_{wc,ult} = \frac{w_{ult} - w_c}{h} \quad \text{for} \quad w_c > w_s \tag{5.3}$$

The resulting tensile stress-strain relationship was given as input for the weakened concrete element rows in FE modelling. For the weakened elements, the strain localization was assumed over an element, so that $h = 20mm$.

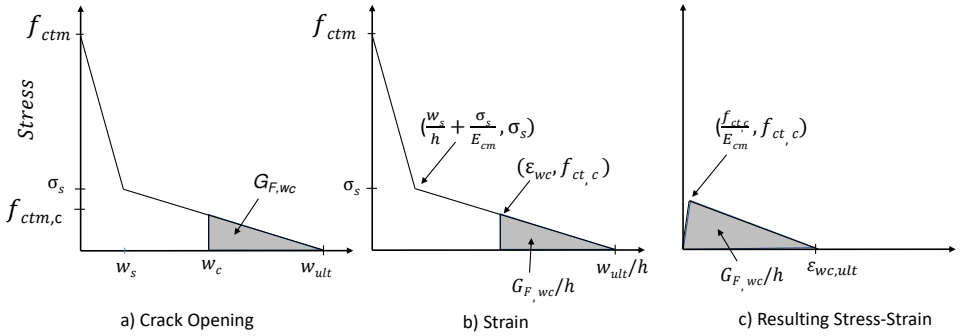

Figure 5.8: Principle of deriving resulting stress-strain curve for weakened concrete using the crack widths, reproduced from Blomfors [49]: a) Bi-linear stress-crack opening relationship [61], b) Stress-strain relationship, using the crack band width h, c) The resulting stress-strain relationship for the weakened elements.

In Figure 5.9, a 3D view of weakened concrete elements corresponding to pre-existing cracks in DN1 beam is shown. In general, the corrosion-induced cracks in the bottom face of the beams, were assumed to extend up to twice the level of the tensile rebars from the beam soffit. Moreover, for cracks at the side face, elements at the level of the tensile rebars were weakened. These cracks were assumed to extend twice the effective cover of the tensile rebar along the width of beam. A detailed presentation of the crack widths, their coordinates and the resulting stress-strain inputs for the cracks corresponding to beams: DN1, DG1 and DC1 are presented in Appendix B.

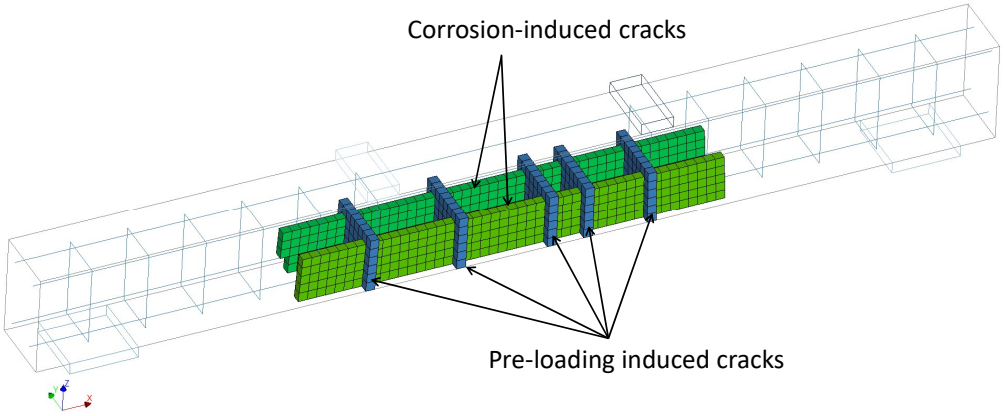

Figure 5.9: 3D view of DN1 beam model with weakened elements for pre-loading and corrosion-induced cracks.

5.9 Incorporation of corrosion damage of reinforcement bars

Yang [18] measured both the average and local corrosion along the tensile rebars using 3D scanning. These measured general and pitting corrosion characteristics were implemented in the FE model by reducing the cross-sectional area of the corroded tensile rebars. The cross-sectional areas of the rebars were reduced by percentage of average corrosion level in the mid 900 mm, see Table 5.5. As the flexural behaviour of the damaged RC beam were highly dependent on the level of pitting corrosion [18], special attention was given to model pitting corrosion. At the locations of major pits, the cross-sectional areas of both bottom rebars were reduced according to the 3D scanned values.

As metioned in chapter 2.3.2, at loading large localized strains are generated at the location of pitting corrosion. The localized strains can be assumed to spread within a certain region, so-called yield length, l_y. To properly describe the deformation capacity at modelling, it is important that the size of the yield length near the pits is described properly. By looking at the equilibrium of a uniaxially loaded bar with varying corrosion levels and a corrosion pit with maximum corrosion level (μ_{max}), it can be found that yielding will not spread outside a zone around the pit where the local corrosion level becomes smaller than μ_p, see Figure 5.10.

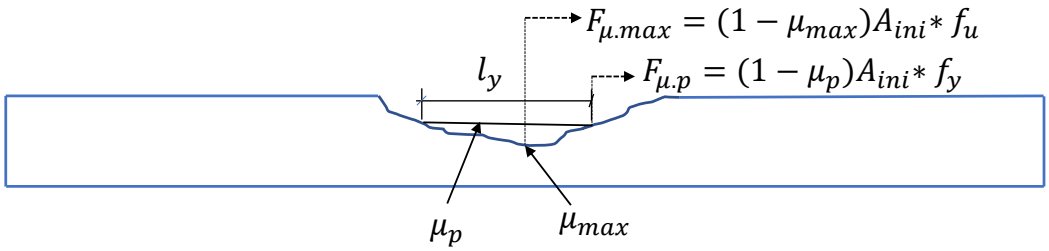

Figure 5.10: Figure showing the forces in a rebar with varying corrosion damages, at a cross-section of maximum corrosion, μ_{max} ($F_{\mu.max}$) and at the cross-section of the end of yield penetration with corrosion level μ_p ($F_{\mu.p}$).

The corrosion level at the end of yield penetration, μ_p, can be derived from equilibrium i.e. by setting $F_{\mu.max} = F_{\mu.p}$. Thusmu_p:

$$\mu_p = 1 - (1 - \mu_{max})f_u/f_y \tag{5.4}$$

where μ_{max} is the maximum corrosion level of the pit:

$$\mu_{max} = 1 - A_{corr.min}/A_{ini} \tag{5.5}$$

Thereafter, the cross-sectional area of rebar at the end of yield penetration, A_p, was calculation by using equation:

$$A_p = (1 - \mu_p)A_{ini} \tag{5.6}$$

where A_{ini} and $A_{corr.min}$ are the cross-sectional area of a rebar before corrosion (nominal area) and minimum cross-sectional area of the rebar at pit after corrosion respectively, f_u and f_y are the ultimate and yield strength of the rebars. The expected yield length (l_y) was estimated by measuring the length of the pit using the 3D scanned rebars, see Figure 5.11. Moreover, Figure 5.11 presents how the average and local corrosion was implemented in the FE model for bar I of the DN1 beam. The explanation regarding the corrosion pits that were considered in FE modelling for all the analyses is presented in Appendix C.

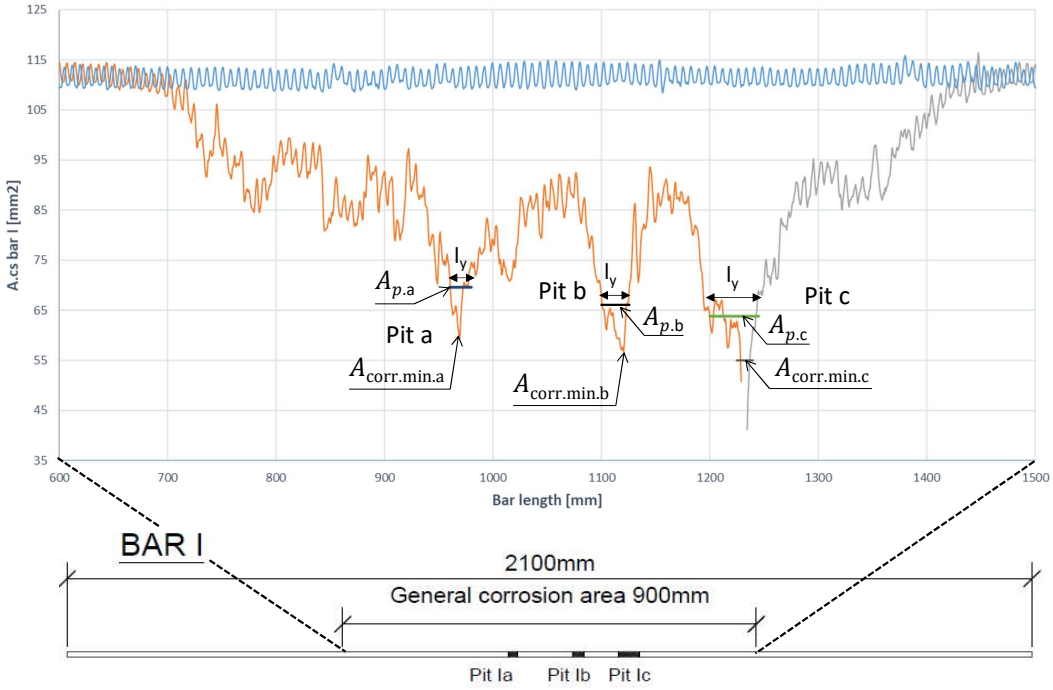

Figure 5.11: Example of how the yield length (l_y) was estimated using the 3D scanning of bar I of DN1 beam and implemented in FE model. $A_{corr.min.a}$, $A_{corr.min.b}$ and $A_{corr.min.c}$ are the minimum cross-sectional areas and $A_{p.a}$, $A_{p.b}$ and $A_{p.c}$ are cross-section areas of a rebar at the end of yield penetration, corresponding to pit, a, b and c respectively. 3D scanned data shows the cross-sectional area of rebar before and after corrosion.

As shown in Figure 5.11 (bottom), the cross-sectional area of the corrosion pits were reduced for the rebar elements at the location of pits in FE model. However, as shown in Table 5.4, the yield length was not always equal to an integer (n) multiple of the element length, l_e. Therefore, to simulate the accurate structural behaviour of the corroded rebars, the strains need to be modified when the yield length is not equal to the integer (n) multiple of the element length. The input for the ultimate and rupture strain of the rebars were modified according to Equation 5.7. The strain corresponding to the ultimate stress in the rebars was considered as

the ultimate strain.

$$\varepsilon_{u.mod} = \varepsilon_u l_y / n l_e \tag{5.7}$$

where ε_u is the initial ultimate strain of the rebars. l_y and l_e are the yield and element length respectively. The ultimate and rupture strain values for the pits are shown in Table 5.4 and Appendix C. In Table 5.4, the input for the corrosion modelling of the pits for the different bars are presented. Moreover, when modelling the non-strengthened corroded beam, DN1, special care was taken to understand the effects of corrosion modelling on the flexural response of the deteriorated beam. Therefore, a number of models were analysed to study the effects of number of pits and how close the pits were to each other in the different rebars. Furthermore, it was investigated how adding "neighbouring" elements to the pit, i.e increasing the yielding length, affects the deformation capacity of the beam. These neighbouring elements were assigned the cross-sectional area of A_p according to Equation 5.6. In Table 5.5, the input for modelling the general corrosion of the bars is presented.

Table 5.4: Input for modelling of the pitting corrosion. Here, I and II represent numbering for the two tensile reinforcement bars, a, b and c represent numbering for major corrosion pits in corresponding tensile rebars.

Bar/Pit	yield length [1] [mm]	x-coordinate [2] [mm]	μ_{max} [3] [%]	$A_{corr.min}$ [mm^2]	$\epsilon_{u.mod}$ [4] [%]	$\epsilon_{rup.mod}$ [5] [%]
DN1						
Ia	20	950-970	45	69.60	8.10	12.0
Ib	25	1090-1110	48	66.12	10.12	15.0
Ic	45	1210-1250	50	63.80	9.11	13.50
IIa	15	970-990	52	61.48	6.10	9.0
IIb	12	1108-1128	44	71.92	4.86	7.20
IIc	75	1190-1270	35	83.28	7.59	11.25
DG1						
Ia	20	970-990	51	62.64	8.10	12.0
Ib	20	1190-1210	51	62.29	8.10	12.0
IIa	40	930-970	33	84.91	8.10	12.0
IIb	20	1335-1355	36	81.55	8.10	12.0
DC1						
Ia	60	910-970	53	56.99	8.10	12.0
Ib	10	1220-1240	55	54.80	4.05	6.0
IIa	20	885-905	55	53.35	8.10	12.0
IIb	20	1210-1230	43	71.96	8.10	12.0

[1] Length of yield penetration estimated from 3D scanned data as shown in Fig 5.11

[2] x-coordinate of pits implemented in FE modelling

[3] μ_{max} - maximum corrosion level

[4] $\epsilon_{u.mod}$ - modified ultimate strain in the pit corresponding to ultimate tensile strength in tensile curve, see Figure 5.5

[5] $\epsilon_{rup.mod}$ - modified rupture strain

Table 5.5: Input for modelling of the general corrosion.

Bar	x-coordinate [1][mm]	rebar area [mm^2]
DN1		
I	600-1500	90.4
II		91.53
DG1		
I	600-1500	88.14
II		93.79
DC1		
I	600-1500	87.01
II		90.04

[1] The general corrosion is applied in these x-coordinates except at the location of pits as mentioned in Table 5.4.

5.10 Modelling of strengthening

The overall layout and dimensions of the FRP strengthening scheme can be seen in section 4.3 and Figure 4.2. The FRPs were modelled as 3D plane stress (membrane) quadrilateral elements (Q12GME elements). The material properties of the GFRP sheet and CFRP plate were assigned as an isotropic material according to Table 5.6. Orthotropic material properties were assigned for the unidirectional vertical U-jackets, see Table 5.7. The stiffness in the weak direction, x-direction in Figure 5.12, of the vertical U-jackets was assumed to be same as the epoxy which was used between the CFRP plate and the concrete. However, for the inclined U-jackets, an isotropic material was used since they were placed at the end of the beams and can be assumed to have minor influence on the flexural capacity. The linear stress-strain relationship of the FRP as shown in Figure 5.13 (a) was implemented in FE analyses as a linear elastic material with a brittle failure when reaching the tensile strength. The tensile strength for the FRP material, in Figure 5.13 (a), was calculated by multiplying the elastic modulus (E_f) with the rupture strain (ε_{fu}). The tensile strength and strain input for the FRP materials are shown in Appendix D.

In Figure 5.12, the meshing of the FRPs for the DG1 beam are presented, where the different geometries are indicated with arrows. The average element size of the FRP was set to 20 mm to align with the concrete. However, a mesh size of 5 mm was chosen for CFRP plate in beam category DC1 as recommended by Kalfat [13].

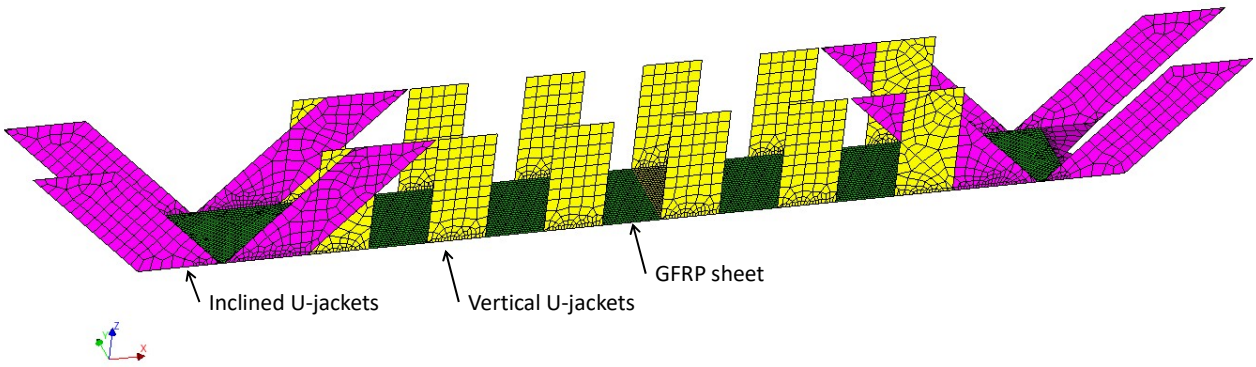

Figure 5.12: Mesh for FRPs in a model of the DG1 beam.

Table 5.6: Dimensions and material properties of isotropic FRP composites [18].

FRP composites	**width×thickness**[mmxmm]	E_f[1][GPa]	ε_{fu}[2][%]	ν[3]
GFRP laminate	150×3.03	20.2	1.82	0.2
CFRP plate	100×1.45	214	1.27	0.2
Inclined CFRP U-jacket	100×2.39	57.6	1.24	0.2

[1] E_f – modulus of elasticity
[2] ε_{fu} - ultimate tensile strain at rupture
[3] ν-poisson's ratio

Table 5.7: Dimensions and material properties of vertical U-jackets (orthotropic CFRP composite) [18].

widht×thickness [1] [mmxmm]	E_{fx}[1][GPa]	E_{fy}[2][GPa]	ε_{fu}[3][%]	ν[4]	G_{xy}[5][GPa]
100×0.797	7.1	57.6	1.24	0.2	5

[1] E_{fx} – modulus of elasticity in x-direction
[2] E_{fy} – modulus of elasticity in y-direction
[3] ε_{fu} – ultimate tensile strain at rupture
[4] ν– Poisson's ratio
[5] G_{xy} – shear modulus

The interface properties between FRPs and concrete were modelled as 3D structural plane interface (Q24IF elements). The non-linear interface properties were modelled by the bi-linear bond stress-slip relationship proposed by Lu et al. [54], see Figure 5.13(b). This bi-linear bond stress-slip relationship is characterized by:

$$\tau = \tau_{max} s/s_0 \quad \text{if} \quad s \leq s_0 \tag{5.8}$$

$$\tau = \tau_{max}(s_f - s/s_f - s_0) \quad \text{if} \quad s_0 < s \leq s_f \tag{5.9}$$

$$\tau = 0 \quad \text{if} \quad s > s_f \tag{5.10}$$

here, s_0 = 0.0611 mm and 0.07 mm, s_f = 0.149 mm and 0.182 mm, τ_{max} = 4.71 MPa and 5.74 MPa for GFRP-concrete and CFRP-concrete interfaces respectively are also based on Lu et al. [54]. For the connection between U-jackets to concrete and U-jackets to CFRP plate, the same bond stress-slip relationships were considered. This assumption was made since no specific interface properties for U-jackets has been found in present literature. However, for the DG1 beam, two different types of analyses were carried out: One with non-linear interface properties for the connection between U-jackets and GFRP sheet, and another one assuming only linear properties, i.e. stiffness corresponding to the inclination of the first segment in the bi-linear relationship. A detailed presentation of the interface properties for all models can be found in Appendix D.

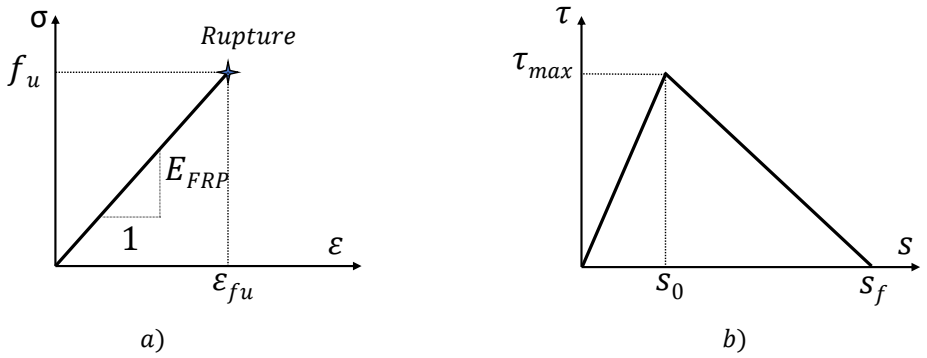

Figure 5.13: FRP modelling parameters: a) Tensile strength- strain relationship b) Bi-linear bond stress-slip relationship for concrete and FRP interface [54]

5.11 Load increment and convergence criteria

The non-linear FEA of RC beams were done by applying deformation controlled loading, as shown in Figure 5.1. For the reference beam, the deformation was applied in 500 steps of 0.05 mm followed by 400 steps of 0.1 mm. For the analyses of deteriorated (DN1) and strengthened (DG1 and DC1) beams, the deformation was applied in 250 steps of 0.02 mm followed by 500 steps of 0.05 mm. The secant iteration, (quasi-Newton iteration) BFGS (Broyden, Fletcher, Goldfarb, and Shanno) method was used to perform iteration and maximum number of iterations was set to 400 to achieve convergence. As suggested by Hendriks, an energy norm of 0.001 and a force norm of 0.01 was implemented as a tolerance limit for convergence in analysis of RN1 and DN1 beams [60]. However, the limit for energy norm was set to 0.01 for the analysis of beams under the DC1 category to achieve the convergence.

6 Results and comparisons

In this chapter, the results from the FE analyses with different modelling choices are presented. The flexural behaviour of four beams; RN1, DN1, DG1 and DC1 are presented and compared with the test results. The effects of pitting corrosion on the deformation and ultimate capacity of the RC beams are also presented in terms of load versus mid span deflection curves. In addition to the tested beams, FE analyses results from different modelling choices, see Table 5.1, are presented to study the effectiveness of the FRP strengthening methods to improve the ultimate load and deformation capacity. In these analyses, the FRP plate/sheet, inclined and vertical U-jackets were applied in stages.

6.1 Flexural behaviour

The flexural behaviour of four different beams (reference, non-strengthened corroded, and corroded but strengthened with GFRP and CFRP) in terms of load versus deflection curves from experiments and FEA are shown in Figure 6.2. The difference between the tests and FEA results in ultimate load capacity and corresponding deflection at mid span of the beams are presented in Table 6.1. The FE analyses were able to capture the same failure mode as in the experiments, see Table 6.1. Failure due to concrete crushing after yielding of tensile reinforcement caused the flexural failure of the reference beam, see Fig 6.3. In the FE analysis of the reference beam, crushing of the concrete was localized into one element row, which agreed with the assumed localization zone, see Figure 6.3. As shown in Figure 6.4, rupture of the bar at the left pit in second (II) bottom rebar caused the brittle failure of the non-strengthened deteriorated beam. The brittle failure due to rupture of the GFRP sheet was found in DG1 beam (FE model DG1_FEA), see Figure 6.5. Furthermore, DC1 beam (FE model DC1_FEA) failed due to a brittle anchorage failure at the end of the CFRP plate, see Figure 6.6.

It is worth to note that the ultimate load capacity of the reference beam (RN1) was 88.8 kN in the FE analysis, which is 14% larger than the test result. This difference was carefully investigated. An analytical calculation was done to calculate the cracking, yielding, and the ultimate load of the reference beam, see Appendix E. As shown in Figure 6.1, the yield and ultimate capacity from the FE analysis of the reference beam matched well with the analytical calculations.

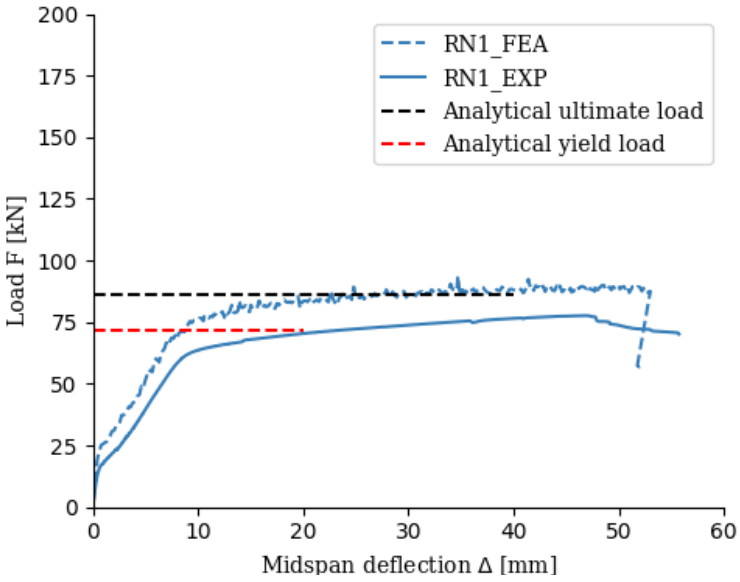

Figure 6.1: A comparison of yielding and ultimate load capacity from test, FE analysis and analytical calculation of reference beam. Here, RN refer to reference beam, FEA and EXP correspond to FE analysis and experiment respectively.

The FE analysis predicted the ultimate capacity and corresponding deformation of 50.8 kN and 17.9 mm for the non-strengthened RC beam (DN1), which was 22% and 10% larger than the test results respectively. The stiffness, yield and ultimate load carrying capacity of the corroded beam was reduced drastically compared to the reference beam, see Figure 6.2.

In both FE analyses and tests, the stiffness and load capacity of the corroded beams were increased substantially after application of the FRP. FE analyses predicted the ultimate capacity of the GFRP and CFRP strengthened beams as 131 kN and 168 kN respectively.

Table 6.1: Ultimate load capacity and failure modes of all beam specimens in experiments (EXP) and FEA.

Specimens	F_u[1][kN]			Δ_u[2][mm]			Failure mode
	EXP	FEA	Ratio	EXP	FEA	Ratio	EXP and FEA
RN1	77.7	88.8	1.14	46.7	53.0	1.13	CC[3]
DN1	41.5	50.8	1.22	16.3	17.9	1.10	RS[4]
DG1	135.8	131.0	0.96	20.1	22.8	1.13	RG[5]
DC1	170.8	168.0	0.98	16.4	14.6	0.89	AC[6]

[1] F_u - Total ultimate load applied.
[2] Δ_u - Corresponding deflection at mid span of beam.
[3] CC - Failure due to concrete crushing
[4] RS - Rupture of steel rebar
[5] RG - Rupture of GFRP sheet
[6] AC - Anchorage failure of CFRP plate

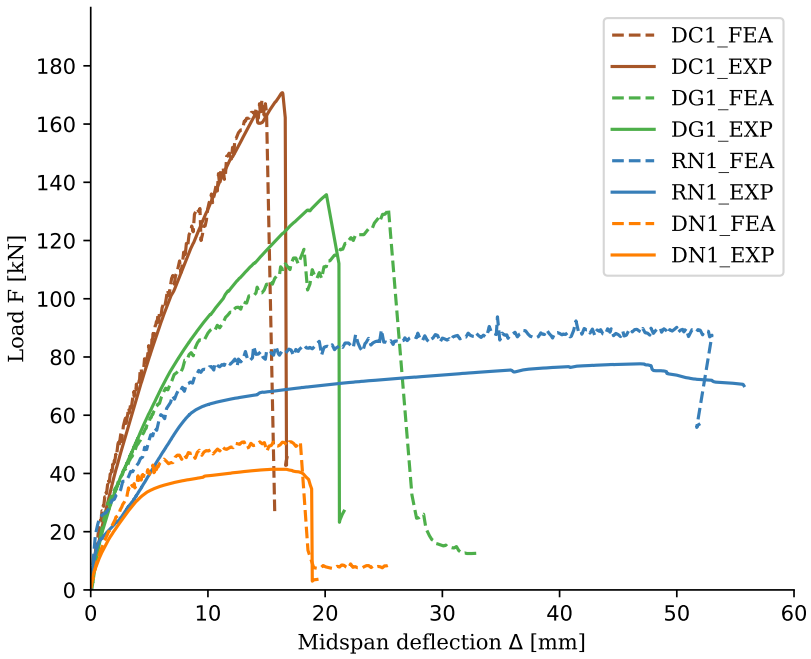

Figure 6.2: Load versus mid-span deflection, FE analyses results are compared with the experimental results.

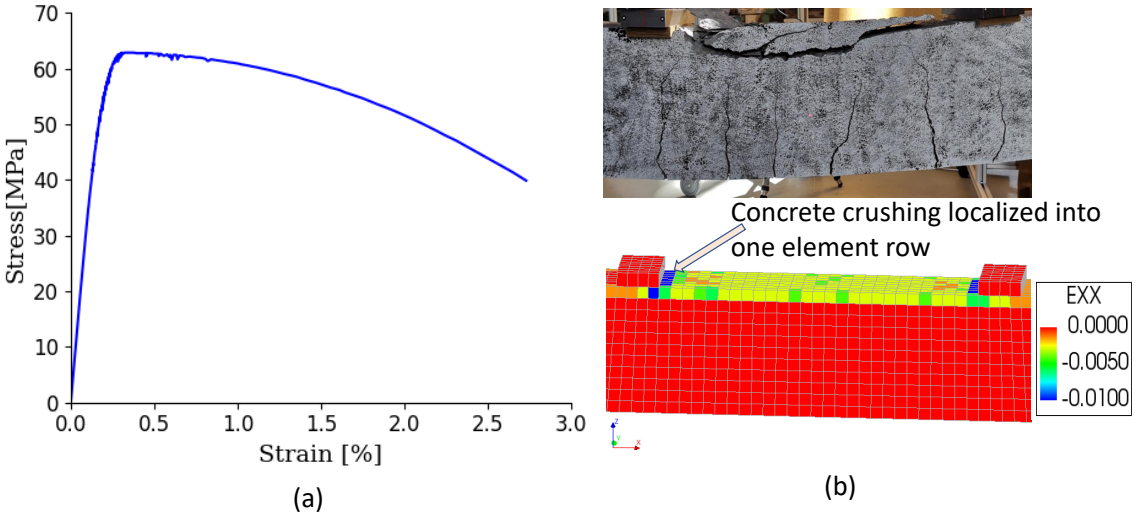

Figure 6.3: The concrete compressive stress vs strain at one of the critical integration points in the analysis of RN1 beam; all elements in a row along the y-direction failed in the crushed state: (a) stress vs strain at the critical integration point associated to the concrete element indicated in (b), (b) Failure of the RN1 beam due to concrete crushing and localization of concrete crushing into one element row, photo from test shows crushing of concrete at failure.

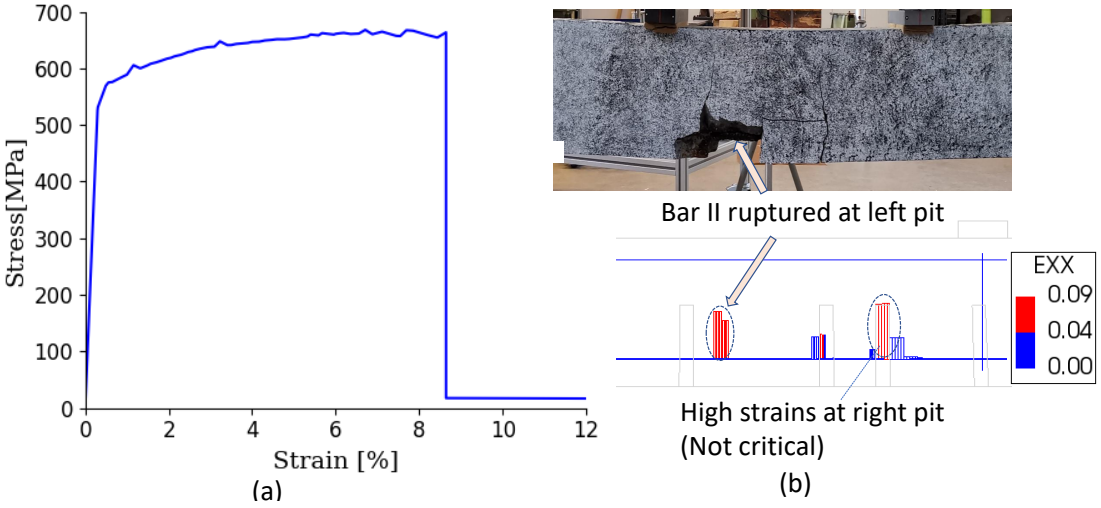

Figure 6.4: The stress versus strain for tensile bar II at the critical pit of DN1 beam: (a) stress versus strain at left pit which initiated failure of the beam, (b) reinforcement element with high strain which initiated failure of the beam due to rupture, photo from experiment shows failure due to rupture of corroded tensile rebar.

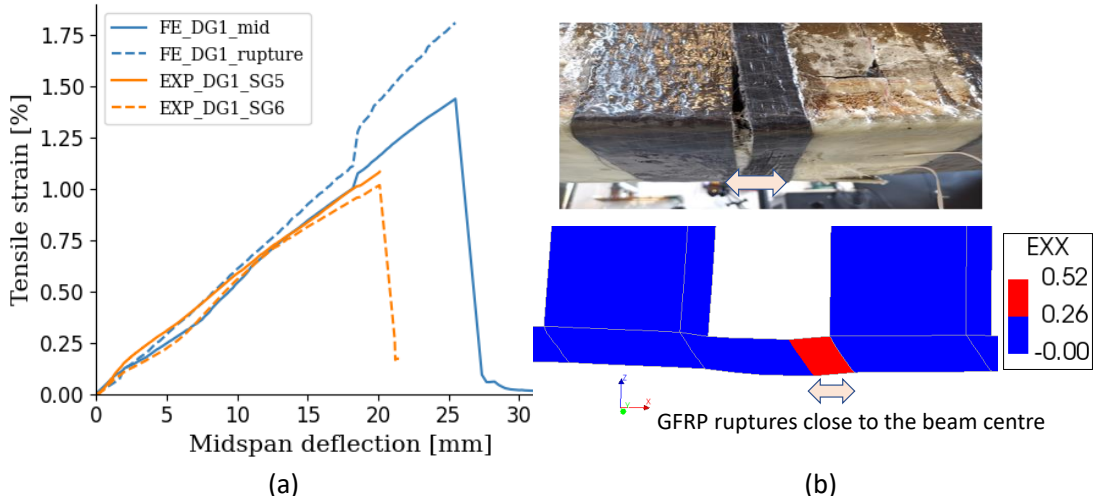

Figure 6.5: The strain development for DG1 beam: (a) the strain versus mid span deflection for GFRP sheet at an integration point corresponding to rupture at mid section, and FE results are compared to the test results, (b) rupture of GFRP sheet in FE analysis compared to GFRP rupture from experiment.

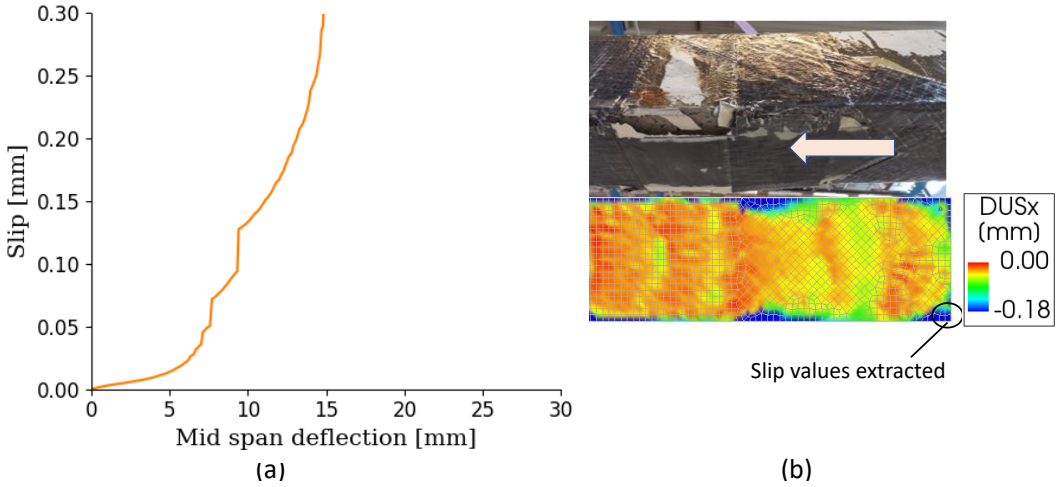

Figure 6.6: (a) End slip versus mid span deflection of CFRP plate in DC1 beam from FE analyses, b) high slip values at the end of CFRP plate indicating anchorage failure as in experiment. The test photo shows slip of the CFRP plate along with inclined U-jackets towards the center of the beam.

6.2 Crack patterns

In this section, the crack pattern at a mid span deflection of 9.39 mm are compared, from DIC measurements during experiments and from FE analyses, see Fig 6.7. As the cracks in FE analyses were localized into one element row, the assumed crack bandwidth was validated. In RN1 beam, the cracks were well distributed over the mid 900 mm region, both in the experiment and the FE analysis. However, the crack width was increased and cracks were localized in the mid section in-between the loading plates of the damaged beam. Both in FE analyses and tests, the application of FRPs suppressed the crack opening effectively, and thereby reduced both the number and width of cracks.

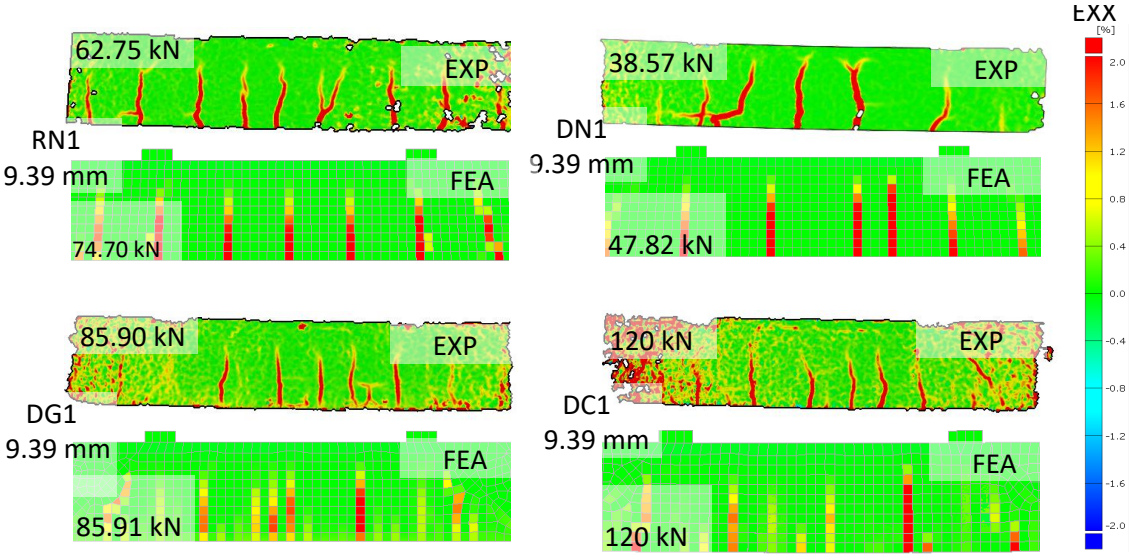

Figure 6.7: Comparison of crack pattern from tests (DIC results) and FE analyses. EXX is the tensile strain along longitudinal direction of the beams. RN1- refernce beam, DN1-damaged but non-strengthened beam, DG1-strengthened with GFRP sheet and DC1-strengthened with CFRP sheet.

6.3 Effects of corrosion

Effects of general and pitting corrosion were studied by analysing the beam of category DN1, see result in Figure 6.8. The general corrosion did not have considerable effects on ultimate and deformation capacity, while it had small influence on stiffness in the initial stage before yielding. However, modelling of the pitting corrosion showed significant effects on deformation capacity of the deteriorated beams. Three different modelling approaches were examined to model the pitting corrosion. The different input parameters such as location of pits, pits area, tensile strength and strain of pits and how the different corrosion pits were chosen in the FE models are shown in chapter 5.9, Table 5.4 and a detailed presentation is shown in Appendix C. It was found that the analysis with three major pits in each tensile rebar (model DN1_FEA) agreed best with the test results. This analysis displayed a higher deformation capacity compared to the other analyses, but almost equal ultimate capacity. The analysis with only one major pit in each bar at a critical section (model DN1P1_FEA) displayed a much less ductile response. Model DN1P1E_FEA was similar to model DN1P1_FEA but with extended yield length by reducing the cross-sectional area of neighbouring elements on both sides of pit Ia and IIa of DN1 beam, see Appendix C. The FE analyses of DN1P1E_FEA model resulted in that the rupture of the rebars did not happen simultaneously, see Figure 6.8.

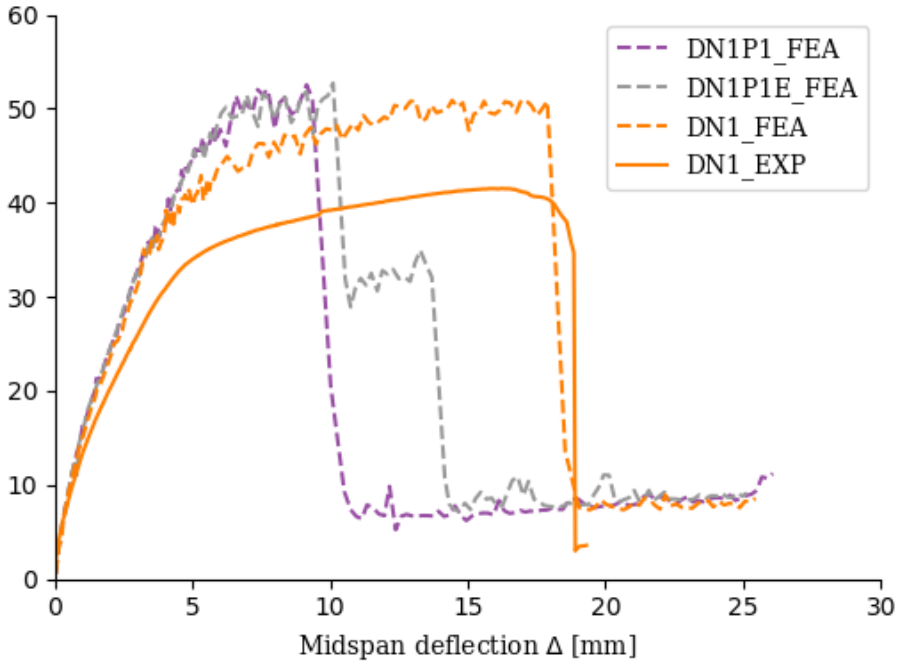

Figure 6.8: Load deflection curves for the DN1 beam with different corrosion modelling, compared to test results.

6.4 Effects of FRP strengthening

6.4.1 Strengthening with GFRP sheet

To study the effect of each FRP component, four different models were analysed with the FRP applied in stages. The first model was non-strengthened, i.e only the corrosion was added to the model. For the second model, the GFRP sheet was applied to the beam soffit. For the third model, the inclined U-jackets were applied to the ends of the GFRP sheet. Finally, the fully strengthened model with all U-jackets was analysed. The results of these analyses can be seen in Figure 6.9. For the fully strengthened model, two different analyses results are presented: One with linear interface properties between U-jackets and GFRP sheet, and the other with non-linear interface properties between U-jackets and GFRP sheet.

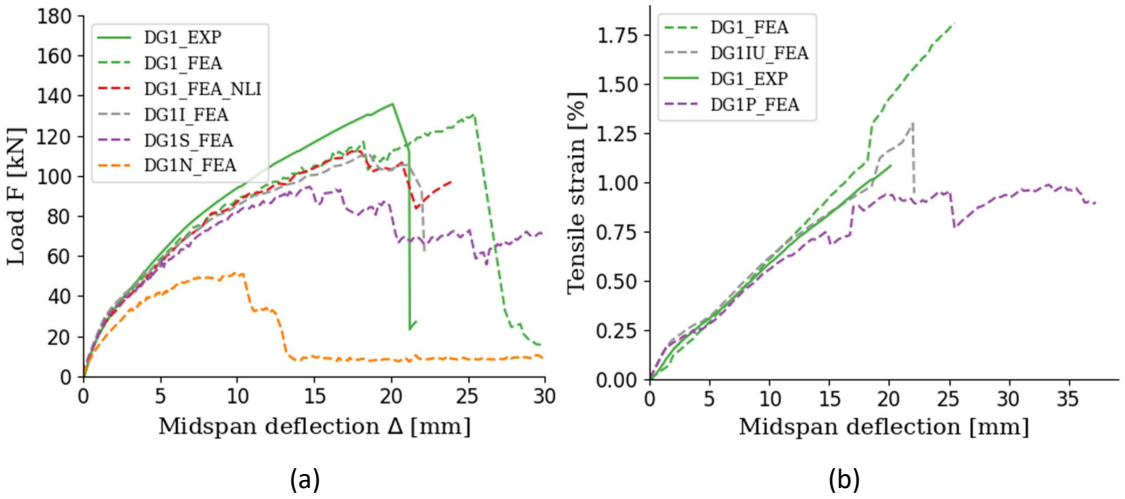

Figure 6.9: (a) Load versus mid span deflection curves for DG1 beam with different modelling choices (b) Strain at an integration point corresponding to the critical section of GFRP sheet vs mid span deflection, for non-strengthened (DG1N_FEA), strengthened with GFRP sheet (DG1S_FEA), inclined U-jackets (DG1I_FEA), with non-linear interface properties and vertical U-jackets (DG1NLI_FEA and DG1_FEA respectively).

In Table 6.2, the effect of each FRP component is presented. Furthermore, the failure mode of each model is presented. Figure 6.10 shows how cracks were suppressed due to the application of the GFRP sheet, inclined and vertical U-jackets.

Table 6.2: Comparison of the ultimate load, corresponding deformation capacity and failure mode of the DG1 beam with different modelling choices.

FEA model	F_u [1] **[kN]**	Δ_u [2] **[mm]**	**Failure mode**
DG1N_FEA: non-strengthened	50.9	10.4	Rebar rupture
DG1P_FEA: strengthened with GFRP sheet	94.5	14.7	Concrete separation
DG1IU_FEA: strengthened with GFRP sheet and inclined U-jackets	111.0	18.6	Anchorage failure of GFRP sheet
DG1NLI_FEA: strengthened with GFRP sheet, inclined and vertical U-jackets non-linear interface properties for U-jackets	112.0	18.0	Anchorage failure of GFRP sheet
DG1_FEA: strengthened with GFRP sheet, inclined and vertical U-jackets linear interface properties for U-jackets	131.0	25.4	GFRP rupture

[1] F_u – Total ultimate load applied
[2] Δ_u – Deflection at mid span of beam corresponding to ultimate load

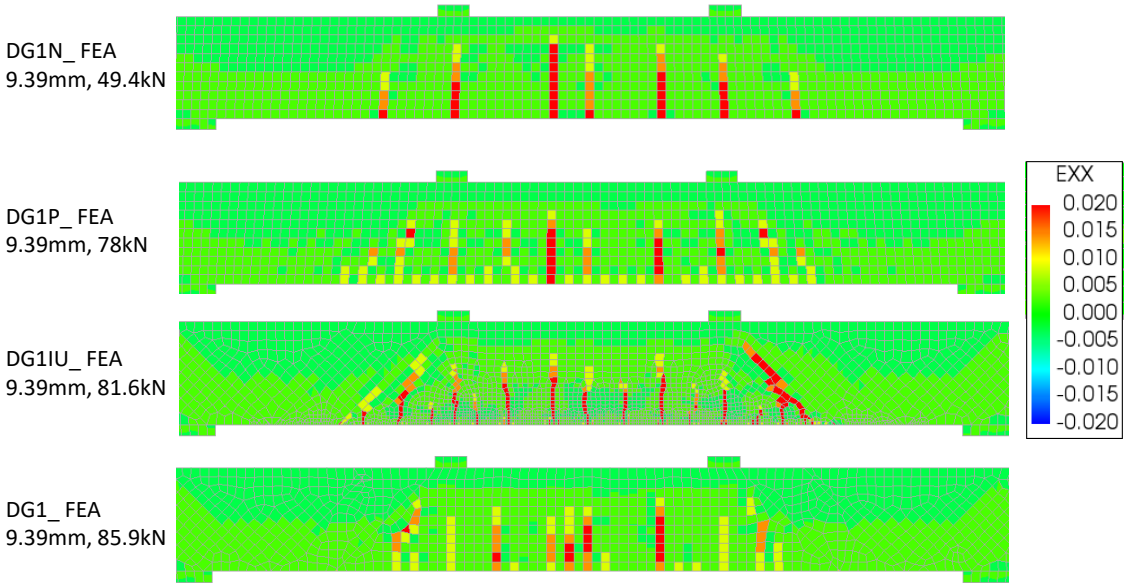

Figure 6.10: Crack pattern of DG1 beam at different stages of FRP strengthening. DG1N_FEA -non-strengthened , DG1S_FEA-strengthened with only GFRP sheet, DG1I_FEA-added inclined U-jackets, and DG1_FEA added vertical U-jackets with linear interface properties between U-jackets and GFRP.

6.4.2 Strengthening with CFRP plate

In this section, the improvement of the load and deformation capacity due to application of CFRP plate, inclined and vertical U-jackets were studied in stages. The load versus mid span deflection curves for different FRP strengthening stages are shown in Figure 6.11 (a). Furthermore, the strain in the CFRP plate was plotted against the mid span deflection to see the utilization of CFRP plate in each strengthening stage, see Fig 6.11 (b). Moreover, the ultimate load-capacity and corresponding deflection in mid span of RC beams are presented in Table 6.3.

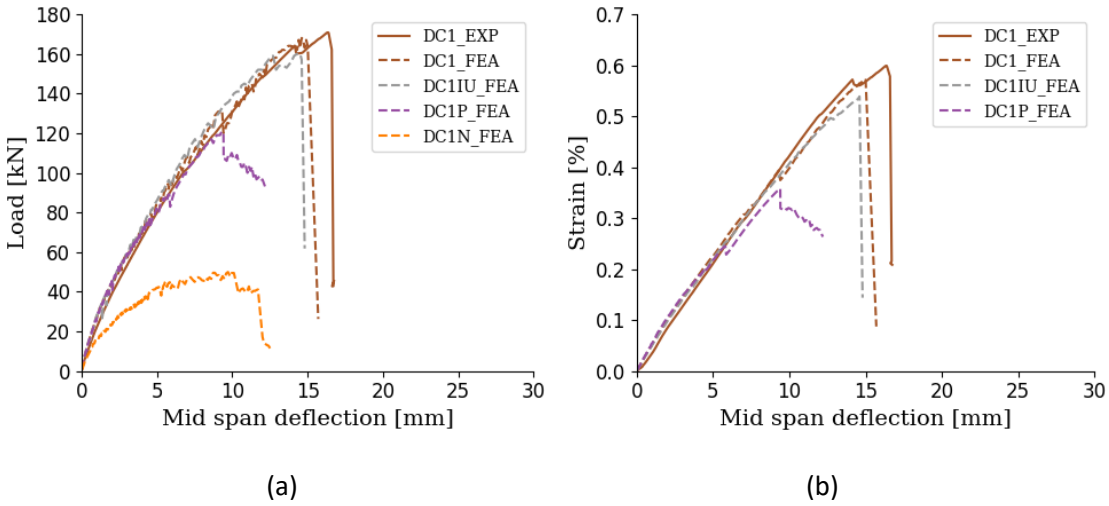

Figure 6.11: (a) Load vs mid span deflection curves for DC1 beam with different modelling choices (b) strain at an integration point corresponding to mid span section vs mid span deflection for non-strengthened (DC1N_FEA), strengthened with CFRP plate (DC1P_FEA), inclined U-jackets added (DC1IU_FEA) and vertical U-jackets added (DC1_FEA), compared with experimental results (DC1_FEA).

The application of CFRP plate at the beam soffit increased the load capacity of the damaged beam to 119 kN, which further increased to 160 kN after application of inclined U-jackets at the end of CFRP plate on the soffit, see Table 6.3. Figure 6.12 shows the crack pattern in different strengthening stages. The crack openings were suppressed effectively due to application of FRP.

Table 6.3: The ultimate load, corresponding mid span deflection and failure mode of the DC1 beam with different modelling choices.

FEA model	F_u [1] **[kN]**	Δ_u [2] **[mm]**	**Failure mode**
DC1N_FEA: non-strengthened	49.6	10.1	Rebar rupture
DC1P_FEA: strengthened with plate	119	11.8	Anchorage failure of CFRP plate
DC1IU_FEA: strengthened with plate and inclined U-jackets	160	14.5	Anchorage failure of CFRP plate
DC1_FEA: strengthened with plate, inclined and vertical U-jackets	168	14.6	Anchorage failure of CFRP plate

[1] F_u – Total ultimate load applied
[2] Δ_u – Deflection at mid span of beam corresponding to the ultimate load

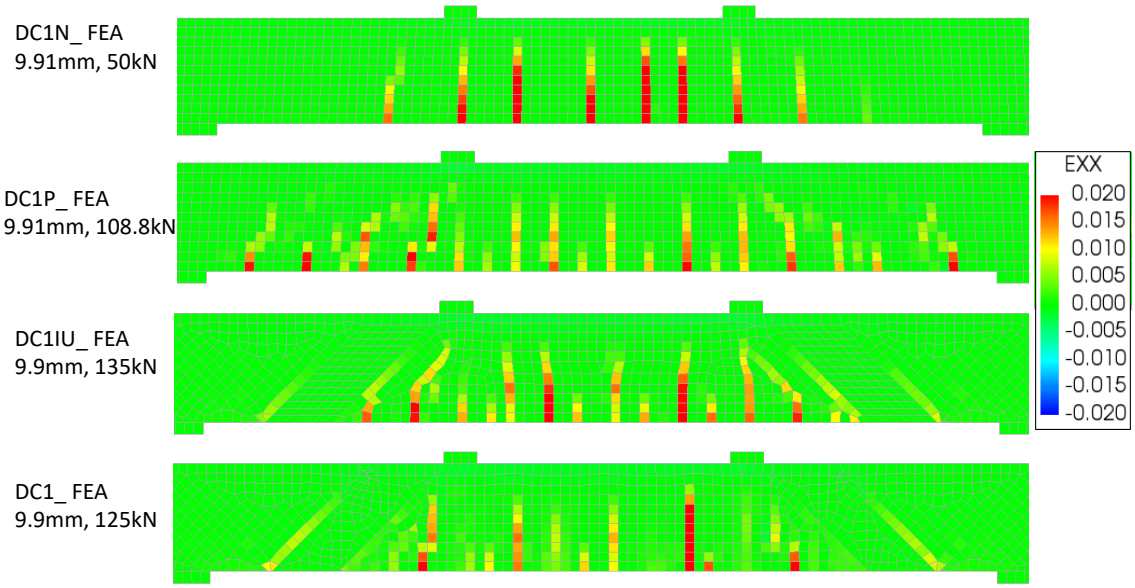

Figure 6.12: Crack pattern of DC1 beam at different amount of FRP strengthening; non-strengthened (DC1N_FEA), strengthened with CFRP plate (DC1P_FEA), inclined U-jackets added (DC1IU_FEA) and vertical U-jackets added (DC1_FEA).

7 Discussion

In general, the FE analyses showed a good correlation to the test results, and they predicted the same failure mode as occurred in the tests for beams RN1, DN1, DG1 and DC1. The overestimated capacity and stiffness of the reference beam compared to the tests is slightly surprising. However, the model was approved as an accurate model since it showed close correlation to the analytically calculated capacities. Furthermore, a comparison was made of the cross-sectional forces from the analysis of the reference beam at a cracked section to the analytical calculation, see Appendix E. A number of possible reasons for the discrepancies to the test results were investigated:

- Placement of the reinforcement bars were double checked in test photos.
- Double checked the nominal diameter and strength for the bottom reinforcement bars.
- Double checked calibration of load cells used at beam testing.

From these investigations, no explanation was found for the discrepancies. However, the analyses of strengthened beams agreed better with the tests results. This could suggest that when the FRPs are the main component providing stiffness for the beams, the results matched the tests better. This may suggest that the geometrical and material properties of the FRPs had a higher accuracy.

The analyses of the DN1 beam were able to predict the same failure mode as in the test, i.e rupture of the pitted rebars. The response of the corroded beam was found to be highly sensitive to the modelling of pitting corrosion. This was studied by trying different modelling choices for the corrosion pits. It was considered important to find a balance between having a simple and practical modelling approach of the corrosion pits and to have a response close to the test results. It was found that the location of pits, yield lengths and number of pits considered were influential to predict the stiffness and deformation capacity of the beams. It is worthwhile to mention that, consideration of all major pits within the both tensile rebars gave higher deformation capacity, close to the test result, by avoiding premature failure of the pits in the rebars. However, only one major pit in each rebar in one critical section resulted in a too brittle failure. Furthermore, it is interesting to note that average corrosion has barely any effect on ultimate and deformation capacity, instead it has small effect on the stiffness before yielding of the tensile rebars.

For the strengthened beams, the interface between the FRPs was assumed to have the same bond-stress slip relationship for interface elements as between FRP and concrete according to Lu et. al., see section 5.10. This method was derived based on the concrete tensile strength and the relation between the width of the concrete and the width of the FRP [54]. This assumption might have some influence on the stiffness of the strengthened beams. Moreover, we noticed that the stiffness of the beams under the category DG1 was affected significantly by the stiffness of the U-jackets and also the interface properties between the GFRP and the U-jackets. For one of the DG1 models, linear interface properties was assumed between the GFRP sheet

and the U-jackets. This assumption was accepted due to; i) the interface properties from Lu et. al was considered to be too conservative, as it is meant for a connection between concrete and FRP, not between FRPs, ii) relatively low slip values at the ends of the GFRP sheet. For the beam in category DC1, the CFRP plate has relatively high stiffness compared to the U-jackets and acted as the main load carrying member. Therefore, the DC1 beam was less influenced by the connection between the CFRP plate and U-jackets, so non-linear interface properties were successfully implemented.

The deformation capacity of the DG1 and DC1 beams was increased, see Figures 6.9 and 6.11, compared to the corresponding non-strengthened beams. Such increase could not be found in the experiments. This may be due to that the deformation capacity is very sensitive to the placement and depth of individual corrosion pits; while they were kept exactly the same in the analyses, they had a variation between specimens in the experiments. This difference was seen in FE analyses because it was possible to make the comparisons of strengthening measures of the same deteriorated beam, which can not be done in tests.

When analysing the beams under the category of DG1, it was found that the failure modes changed depending on how many of the FRP components were applied. When only the GFRP sheet was applied, the failure was caused by concrete separation due to high tensile forces at the ends of the sheet. When the inclined U-jackets were applied, the failure mode changed to anchorage failure. It is important to note that a non-linear interface property was used between the inclined U-jackets and the GFRP sheet for this analysis, which might be conservative as mentioned in a previous paragraph. When applying the intermediate U-jackets and linear interface properties between U-jackets and GFRP sheet, the failure mode changed to GFRP sheet rupture. The utilization of the GFRP sheet was 54% for the beam with GFRP sheet only; this increased to 71% after application of inclined U-jackets at the end of GFRP sheet with non-linear interface properties between FRP connections.

For the beams under category DC1, it was found that the mesh size of the CFRP plate was of high importance for the response. Mesh size of 5mm was required to capture the high stress concentration at the vicinity of CFRP and concrete interface. When applying a course mesh, high stress concentrations resulted in a premature anchorage failure of the beam. The utilization of the CFRP plate was 28% for the beam with CFRP plate only; this increased to 41% after application of inclined U-jackets at the end of CFRP plate. The stiff CFRP plate had brittle anchorage failure limiting the utilization of its high tensile strength. The inclined U-jackets delayed the anchorage failure of the CFRP plate by providing extra anchorage to the end of CFRP plate. It is interesting to note that the application of intermediate U-jackets had negligible influence on load and deformation capacity for the beam with CFRP plate. A reason for this might be since the CFRP plate has high stiffness in comparison to U-jackets and the studied beam did not have significant corrosion cracks. It can also be viewed as the inclined and vertical U-jackets were not mobilized effectively in the experiments, which needs further research.

8 Conclusions and future research

8.1 Conclusion

In this work, finite element analyses were carried out to study the effectiveness of FRP strengthening methods regarding the load-carrying and deformation capacity in bending of corrosion damaged RC beams. The FE analyses results were compared and validated with test results. Pre-loading and corrosion-induced cracks were incorporated by reducing the tensile strength of concrete elements corresponding to crack locations. Pitting and average corrosion were implemented by reducing the cross-sectional area of rebars at the location of corrosion. From this work, the following conclusions were drawn:

- Non-linear finite element analysis were able to predict the structural behaviour of damaged and strengthened RC beams in a reliable way. The FE analyses were useful to study the effectiveness of strengthening methods by applying FRP components in stages, which was not done in the experiments.
- Modelling of the corrosion pits was sensitive and crucial to predict the deformation capacity and failure mode of the beam, while ultimate load remained unaffected regardless of how the pits were modelled. Due to the pitting corrosion of tensile rebars, the ultimate and deformation capacity of the deteriorated beam were reduced substantially. For the non-strengthened beam, the ultimate and deformation capacity was limited to 57% and 34% of the reference beam respectively.
- The average corrosion level was not influential on the load and deformation capacity, while it had a small effect on the stiffness before yielding of the tensile rebars.
- The ultimate load capacity and stiffness of the corrosion damaged RC beams strengthened with CFRP and GFRP was increased significantly. The application of FRP was able to suppress the opening of cracks effectively.
- For the studied beam geometry and corrosion damage, the application of the intermediate vertical U-jackets were not influential to improve the flexural performance of the damaged beams.
- The interface properties between FRP to concrete and between the FRPs in the FE model are important to accurately predict the load-carrying capacity and failure mode of the strengthened beams.
- The interface properties between the GFRP sheet and U-jackets were more influential in predicting the flexural behaviour of the GFRP strengthened beam than the interface properties between the CFRP plate and U-jackets.

8.2 Suggestions for future research

The analyses model were validated with results from a limited number of artificially corroded tests. Thus, to get more reliable results, FE analyses need to be calibrated with naturally corroded tested beams.

In the current study, corrosion-induced cracks were narrow and located in mid region only. It would be interesting to analyse specimens with wider and longer corrosion-induced cracks to investigate if this would increase the demand for intermediate vertical U-jackets. Furthermore, in the present study, the extension of cracks from surface to inside the concrete beams was not clear; more accurate techniques to measure this would be preferred.

To further evaluate the effectiveness of the strengthening methods, it would be necessary to study beams with varying dimensions, corrosion patterns and levels, spacing and dimensions of FRP.

Bibliography

[1] Al-Mahaidi, Riadh and Kalfat, Robin. Introduction. In *Rehabilitation of Concrete Structures with Fiber-Reinforced Polymer*, number 2004, pages 1–5. Matthew Deans, 2018.

[2] Zhou, Y., Gencturk, B., Willam, K., and Attar, A. Carbonation-Induced and Chloride-Induced Corrosion in Reinforced Concrete Structures. *Journal of Materials in Civil Engineering*, 27(9):04014245, 2015.

[3] Fernandez, Ignasi, Herrador, Manuel F., Marí, Antonio R., and Bairán, Jesús Miguel. Structural effects of steel reinforcement corrosion on statically indeterminate reinforced concrete members. *Materials and Structures/Materiaux et Constructions*, 49(12):4959–4973, 2016.

[4] Chen, E., Berrocal, Carlos G., Fernandez, Ignasi, Löfgren, Ingemar, and Lundgren, Karin. Assessment of the mechanical behaviour of reinforcement bars with localised pitting corrosion by Digital Image Correlation. *Engineering Structures*, 219(May):110936, 2020.

[5] Lundgren, K. Bond between ribbed bars and concrete. Part 1: Modified model. *Magazine of Concrete Research*, 57(7):371–382, 2005.

[6] Al-Mahaidi, Riadh and Kalfat, Robin. Methods of Structural Rehabilitation and Strengthening. In *Rehabilitation of Concrete Structures with Fiber-Reinforced Polymer*, number 2004, pages 7–13. Matthew Deans, 2018.

[7] El Maaddawy, Tamer and Soudki, Khaled. Carbon-Fiber-Reinforced Polymer Repair to Extend Service Life of Corroded Reinforced Concrete Beams. *Journal of Composites for Construction*, 9(2):187–194, 2005.

[8] Bergström, Markus. *Assessment of Existing Concrete Bridges. Bending stiffness as a performance indicator*. PhD thesis, Luleå University of Technology, 2009.

[9] Al-Saidy, A. H. and Al-Jabri, K. S. Effect of damaged concrete cover on the behavior of corroded concrete beams repaired with CFRP sheets. *Composite Structures*, 93(7):1775–1786, 2011.

[10] Al-Saidy, A. H., Saadatmanesh, H., El-Gamal, S., Al-Jabri, K. S., and Waris, B. M. Structural behavior of corroded RC beams with/without stirrups repaired with CFRP sheets. *Materials and Structures/Materiaux et Constructions*, 49(9):3733–3747, 2016.

[11] Triantafyllou, Garyfalia G., Rousakis, Theodoros C., and Karabinis, Athanasios I. Effect of patch repair and strengthening with EBR and NSM CFRP laminates for RC beams with low, medium and heavy corrosion. *Composites Part B: Engineering*, 133:101–111, 2018.

[12] Fu, B., Tang, X. T., Li, L. J., Liu, F., and Lin, G. Inclined FRP U-jackets for enhancing structural performance of FRP-plated RC beams suffering from IC debonding. *Composite Structures*, 200(June 2017):36–46, 2018.

[13] Kalfat, R. and Al-Mahaidi, R. Numerical and Experimental Validation of FRP Patch Anchors Used to Improve the Performance of FRP Laminates Bonded to Concrete. *Journal of Composites for Construction*, 18(3):1–10, 2014.

[14] Qapo, Michael, Dirar, Samir, Yang, Jian, and Elshafie, Mohammed Z.E.B. Nonlinear finite element modelling and parametric study of CFRP shear-

strengthened prestressed concrete girders. *Construction and Building Materials*, 76:245–255, 2015.

[15] Zidani, M'hamed Berrezoug, Belakhdar, Khalil, Tounsi, Abdelouahed, and Adda Bedia, El Abbes. Finite element analysis of initially damaged beams repaired with FRP plates. *Composite Structures*, 134:429–439, 2015.

[16] Wu, Yu Fei, Wang, Zhenyu, Liu, Kang, and He, Wei. Numerical analyses of hybrid-bonded FRP strengthened concrete beams. *Computer-Aided Civil and Infrastructure Engineering*, 24(5):371–384, 2009.

[17] DIANA FEA. Reinforced concrete beam under static load : simulation of an experimental test.

[18] Yang, Jincheng. *Strengthening reinforced concrete structures with FRP composites*. PhD thesis, Chalmers University of Technology, 2021.

[19] Täljsten, Björn, Blanksvärd, Thomas, and Sas, Gabriel. *Kompositförsärkning av betong*.

[20] Pham, Huy and Al-Mahaidi, Riadh. Assessment of available prediction models for the strength of FRP retrofitted RC beams. *Composite Structures*, 66(1-4):601–610, 2004.

[21] Hanjari, Kamyab Z., Kettil, Per, and Lundgren, Karin. Modelling the structural behaviour of frost-damaged reinforced concrete structures. *Structure and Infrastructure Engineering*, 9(5):416–431, 2013.

[22] Al-Mahaidi, Riadh and Kalfat, Robin. Strengthening Members in Flexure Using FRP. In *Rehabilitation of Concrete Structures with Fiber-Reinforced Polymer*, pages 25–119. Matthew Deans, 2018.

[23] Du, Y. G., Clark, L. A., and Chan, A. H.C. Residual capacity of corroded reinforcing bars. *Magazine of Concrete Research*, 57(3):135–147, 2005.

[24] Du, Y. G., Clarkt, L. A., and Chan, A. H.C. Effect of corrosion on ductility of reinforcing bars. *Magazine of Concrete Research*, 57(7):407–419, 2005.

[25] Lundgren, K. Effect of corrosion on the bond between steel and concrete: An overview. *Magazine of Concrete Research*, 59(6):447–461, 2007.

[26] FIB. fib Model Code for Concrete Structures 2010. 2010.

[27] Cairns, J., & Millard, S. Reinforcement corrosion and its effect on residual strength of concrete structures. page 12pp, London, 1999.

[28] Zhang, Weiping, Song, Xiaobin, Gu, Xianglin, and Li, Shibin. Tensile and fatigue behavior of corroded rebars. *Construction and Building Materials*, 34:409–417, 2012.

[29] Apostolopoulos, C. A. and Papadakis, V. G. Consequences of steel corrosion on the ductility properties of reinforcement bar. *Construction and Building Materials*, 22(12):2316–2324, 2008.

[30] Stewart, Mark G. and Al-Harthy, Ali. Pitting corrosion and structural reliability of corroding RC structures: Experimental data and probabilistic analysis. *Reliability Engineering and System Safety*, 93(3):373–382, 2008.

[31] Of, Rends and Bonacci, By J F. B Ehavioral T Rends of Rc B Eams S Trengthened E Xternally B Onded Frp. *Journal of Composites for Construction*, 5(May):102–113, 2001.

[32] Al-Saidy, A. H. and Al-Jabri, K. S. Effect of damaged concrete cover on the behavior of corroded concrete beams repaired with CFRP sheets. *Composite Structures*, 93(7):1775–1786, 2011.

[33] Siddika, Ayesha, Mamun, Md Abdullah Al, Alyousef, Rayed, and Amran, Y. H.Mugahed. Strengthening of reinforced concrete beams by using fiber-reinforced polymer composites: A review. *Journal of Building Engineering*, 25(May):100798, 2019.

[34] Benjeddou, Omrane, Ouezdou, Mongi Ben, and Bedday, Aouicha. Damaged RC beams repaired by bonding of CFRP laminates. *Construction and Building Materials*, 21(6):1301–1310, 2007.

[35] Fayyadh, Moatasem M. and Abdul Razak, Hashim. Assessment of effectiveness of CFRP repaired RC beams under different damage levels based on flexural stiffness. *Construction and Building Materials*, 37:125–134, 2012.

[36] Xie, Jian He and Hu, Ruo Lin. Experimental study on rehabilitation of corrosion-damaged reinforced concrete beams with carbon fiber reinforced polymer. *Construction and Building Materials*, 38:708–716, 2013.

[37] Linwang, Su, Jian, Cai, Qingjun, Chen, Guobao, Li, and Juan, Zhao. Investigation on the Flexural Behavior of Corroded Concrete Beams Repaired by CFRP Sheet Under Different Corrosion Levels. *The Open Civil Engineering Journal*, 10(1):598–614, 2016.

[38] Al-Saidy, A. H., Al-Harthy, A. S., Al-Jabri, K. S., Abdul-Halim, M., and Al-Shidi, N. M. Structural performance of corroded RC beams repaired with CFRP sheets. *Composite Structures*, 92(8):1931–1938, 2010.

[39] Fu, B., Teng, J. G., Chen, J. F., Chen, G. M., and Guo, Y. C. Concrete Cover Separation in FRP-Plated RC Beams: Mitigation Using FRP U-Jackets. *Journal of Composites for Construction*, 21(2):04016077, 2017.

[40] Belletti, Beatrice, Damoni, Cecilia, Hendriks, Max A.N., and de Boer, Ane. Validation of the Guidelines for Nonlinear Page 2 of 129 Finite Element Analysis of Concrete Structures. (June):129, 2017.

[41] Mathern, Alexandre and Yang, Jincheng. A practical finite element modeling strategy to capture cracking and crushing behavior of reinforced concrete structures. *Materials*, 14(3):1–26, 2021.

[42] Blomfors, Mattias, Zandi, Kamyab, Lundgren, Karin, and Coronelli, Dario. Engineering bond model for corroded reinforcement. *Engineering Structures*, 156:394–410, 2018.

[43] Earij, Alrazi, Alfano, Giulio, Cashell, Katherine, and Zhou, Xiangming. Nonlinear three–dimensional finite–element modelling of reinforced–concrete beams: Computational challenges and experimental validation. *Engineering Failure Analysis*, 82(September):92–115, 2017.

[44] Blomfors, Mattias, Lundgren, Karin, and Zandi, Kamyab. Incorporation of pre-existing longitudinal cracks in finite element analyses of corroded reinforced concrete beams failing in anchorage. Technical Report 0, 2020.

[45] Plos, Mario, Johansson, Morgan, Zandi, Kamyab, and Shu, Jiangpeng. Recommendations for Assessment of Reinforced Concrete Slabs Enhanced structural analysis with the finite element method. Technical report, 2019.

[46] Foster, S. J., Budiono, B., and Gilbert, R. I. Rotating crack finite element model for reinforced concrete structures. *Computers and Structures*, 58(1):43–50, 1996.

[47] R.V., Milford and Schnobrich, Wc. Computational strategies for nonlinear and fracture mechanics problems. *Comput. Struct*, 20(1):225–234, 1985.

[48] Biondini, Fabio and Vergani, Matteo. Deteriorating beam finite element for nonlinear analysis of concrete structures under corrosion. *Structure and Infrastructure Engineering*, 11(4):519–532, 2015.

[49] Blomfors, Mattias, G. Berrocal, Carlos, Lundgren, Karin, and Zandi, Kamyab. Incorporation of pre-existing cracks in finite element analyses of reinforced concrete beams without transverse reinforcement. *Engineering Structures*, 229:111601, 2021.

[50] Mahjoub, Reza and Hashemi, Seyed Hamid. Finite element analysis of RC beams strengthened with FRP sheets under bending. *Australian Journal of Basic and Applied Sciences*, 4(5):773–778, 2010.

[51] Cui, Shiqi, Wang, Jinshan, Shi, Lei, and Liu, Yan. Test and FEM analysis of debonding failure of RC beam strengthened with CFRP. *Journal of Reinforced Plastics and Composites*, 28(17):2151–2160, 2009.

[52] Freddi, F. and Savoia, M. Analysis of FRP-concrete debonding via boundary integral equations. *Engineering Fracture Mechanics*, 75(6):1666–1683, 2008.

[53] Lu, X. Z., Ye, L. P., Teng, J. G., and Jiang, J. J. Meso-scale finite element model for FRP sheets/plates bonded to concrete. *Engineering Structures*, 27(4):564–575, 2005.

[54] Lu, X. Z., Teng, J. G., Ye, L. P., and Jiang, J. J. Bond-slip models for FRP sheets/plates bonded to concrete. *Engineering Structures*, 27(6):920–937, 2005.

[55] Wang, Jialai and Zhang, Chao. Nonlinear fracture mechanics of flexural-shear crack induced debonding of FRP strengthened concrete beams. *International Journal of Solids and Structures*, 45(10):2916–2936, 2008.

[56] Rots, J G. Computational {M}odeling of {C}oncrete {F}racture. 1988.

[57] Cornelissen, H.A.W., Hordijk, D.A., and Reinhardt, H.W. Cornelissen, Hordijk, Reinhardt - 1986.pdf, 1986.

[58] Feenstra, P. H. *Computational aspects of biaxial stress in plain and reinforced concrete.* PhD thesis, Delft University of Technology., 1993.

[59] F. J. Vecchio and M. P. Collins. Vecchio. *Chinese Science Bulletin*, 39(15):1380–1383, 1994.

[60] Hendriks, Max A.N., de Boer, Ane, and Belletti, Beatrice. Guidelines for nonlinear finite element analysis of concrete structures: Girder Members - Report RTD:1016:2012. 2012.

[61] Wittmann, F. H., Rokugo, K., Brühwiler, E., Mihashi, H., and Simonin, P. Fracture energy and strain softening of concrete as determined by means of compact tension specimens. *Materials and Structures*, 21(1):21–32, 1988.

[62] Yang, Jincheng, Haghani, Reza, and Al-Emrani, Mohammad. Innovative prestressing method for externally bonded CFRP laminates without mechanical anchorage. *Engineering Structures*, 197, 2019.

Appendix A: Reinforcement Properties

Table A.1: Reinforcement properties according to tensile test conducted by Yang [18].

Steel reinforcement	E_s [1]**[GPa]**	f_{sy} [2]**[MPa]**	f_{su} [3]**[MPa]**	ε_{su} [4]**(%)**
Tensile rebar, ϕ12	191	570	661	8.1
Compression rebar, ϕ10	200	528	630	8.9
Stirrups, ϕ8	202	531	654	9.6

[1] E_s - elastic modulus,
[2] f_{sy} - yield strength,
[3] f_{su} - ultimate tensile strength,
[4] ϵ_{su} - ultimate tensile strain.

Table A.2: Properties of the rebars which were given as input in FE modelling. For the pitted rebars, ultimate and rupture strain were modified, see Appendix C. The strain corresponding to the ultimate tensile strength i.e 661 MPa for bottom rebar, was considered as ultimate strain.

Tensile rebar (ϕ12)			**Compression rebar** (ϕ10)			**Stirrups** (ϕ8)		
σ[1] [MPa]	ε[2] [%]	E.s[3] [GPa]	σ[1] [MPa]	ε[2] [%]	E.s[3] [GPa]	σ[1] [MPa]	ε[2] [%]	E.s[3] [GPa]
0	0	191	0	0	200	0	0	202
530	0.298		505	0.3		531	0.26	
570	0.5		530	0.5		654	9.6	
605	1.5		560	1.3				
635	2.78		590	2.5				
661	8.1		620	5				
650	12		630	8.9				
0	12.01		625	12				

[1] σ - tensile strength
[2] ε - tensile strain
[3] E_s - elastic modulus

Appendix B: Incorporation of Pre-existing Cracks

This appendix presents the supplementary data for pre-loading and corrosion induced cracks that were used in FE modelling and which has not been presented in the report.

1. **Pre-loading induced cracks**
   In Table B.1, the pre-loading induced cracks measured by Yang are shown [18]. The crack width measured at pre-loading at the tensile edge of the beam (w.25kN.edge) were implemented in FE modelling. Based on the bilinear mode-I-stress-to-crack relation as mentioned in section 5.8, the resulting stress and strain values for the corresponding concrete elements are shown in Table B.2, B.3 and B.4.

Table B.1: Position and crack width of pre-loading induced cracks that were considered in FE modelling of the beams under the category DN1, DG1 and DC1.

Crack number	x-coordinate [mm]	Crack width [mm] (w.25kN.edge)
DN1		
1	735	0.05
2	937	0.20
3	1125	0.20
4	1215	0.04
5	1337	0.09
DG1		
1	755	0.057
2	970	0.115
3	1045	0.135
4	1210	0.150
5	1360	0.083
DC1		
1	758	0.013
2	865	0.054
3	942	0.131
4	1075	0.172
5	1224	0.070
6	1350	0.070

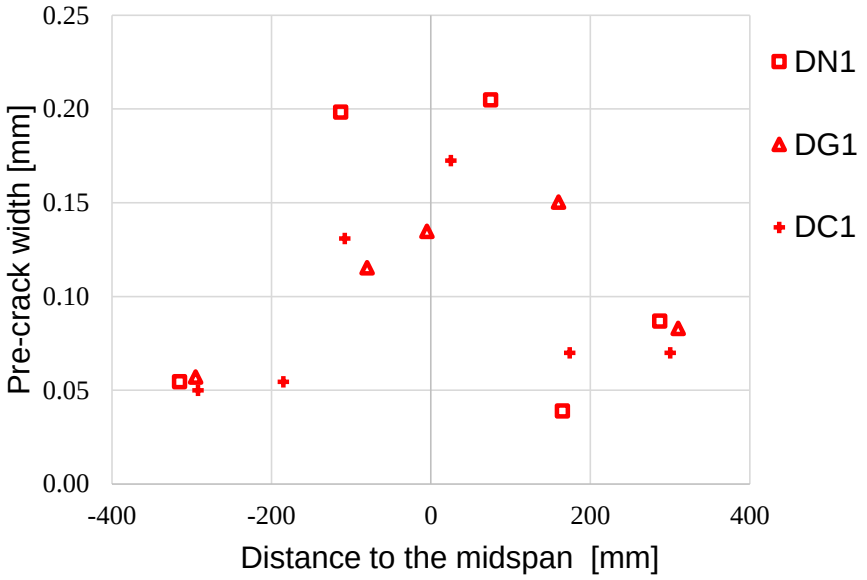

Figure B.1: Plot showing the pre-loading induced crack width.

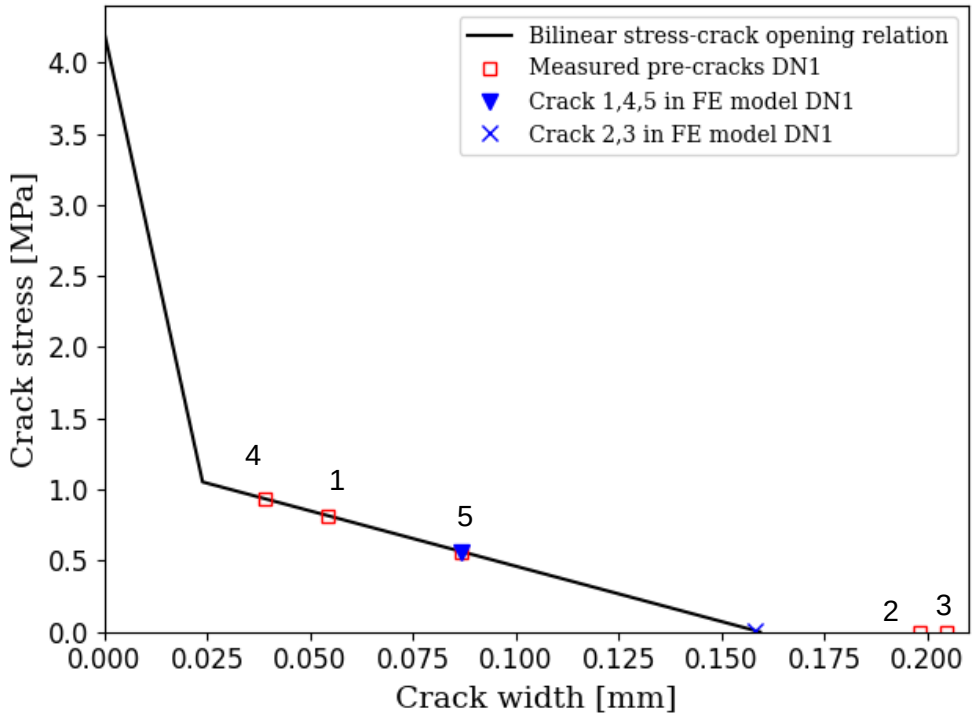

Figure B.2: Crack stress vs crack widths for beams under the category of DN1 and simplified crack widths for the FE model.

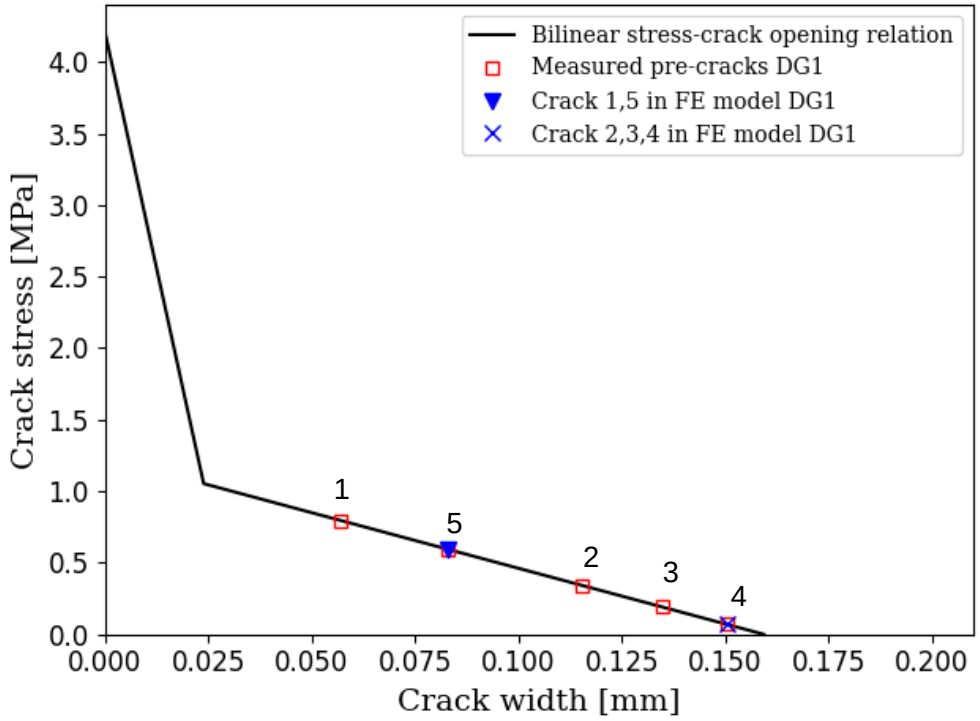

Figure B.3: Crack stress vs crack widths for the beams under the category DG1 and simplified crack widths for the FE model.

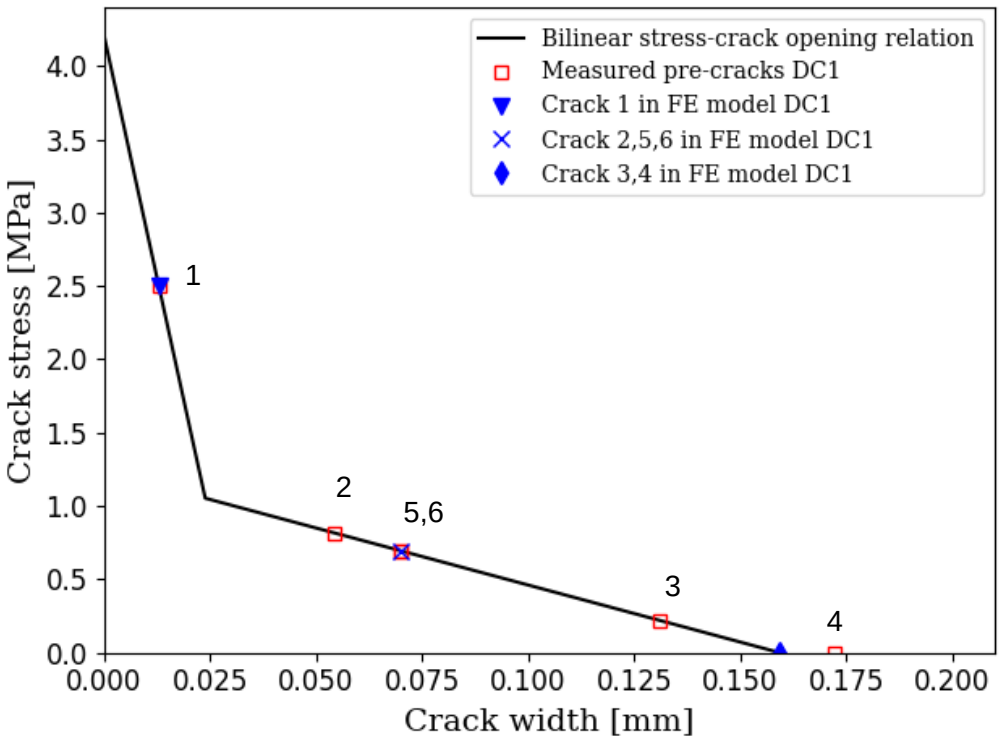

Figure B.4: Crack stress vs crack widths for the beams under the category DC1 and simplified crack widths for the FE model.

Table B.2: Resulting tensile strength and strain for the concrete elements at the location of pre-loading cracks corresponding to beam category DN1.

DN1			
Cracks 1, 4 and 5		Cracks 2 and 3	
Stress [MPa]	Strain [-]	Stress [MPa]	Strain [-]
0	0	0	0
0.564	1.69E-05	0.01	3.0E-07
0	3.63E-03	0	6.431E-05

Table B.3: Resulting tensile strength and strain for the concrete elements at the location of pre-loading cracks corresponding to beam category DG1.

DG1			
Cracks 1 and 5		Cracks 2, 3 and 4	
Stress [MPa]	Strain [-]	Stress [MPa]	Strain [-]
0	0	0	0
0.594	1.78E-05	0.07	4.52E-06
0	3.82E-03	0	4.5E-04

Table B.4: Resulting tensile strength and strain for the concrete elements at the location of pre-loading cracks corresponding to beam category DC1.

DC1					
Crack 1		Cracks 2, 5 and 6		Cracks 3 and 4	
Stress [MPa]	Strain [-]	Stress [MPa]	Strain [-]	Stress [MPa]	Strain [-]
0	0	0	0	0	0
2.50	7.51E-05	0.695	2.09E-05	0.001	3.00E-08
0	7.32E-03	0	4.47E-03	0	6.43E-06

2. **Corrosion induced cracks**
   In the following, the location and widths of the corrosion induced cracks are presented. These cracks were measured by Yang [62] in bottom, front and back side of the beam at the location of tensile reinforcements. As indicated by the horizontal red lines in Fig. B.5, B.6 and B.7, the measured longitudinal corrosion cracks were generalized into uniform longitudinal cracks in FE modelling. The respective resulting stress and strain values are shown in Table B.6. Moreover, Table B.5 shows the widths of the corrosion induced cracks measured by Yang [18].

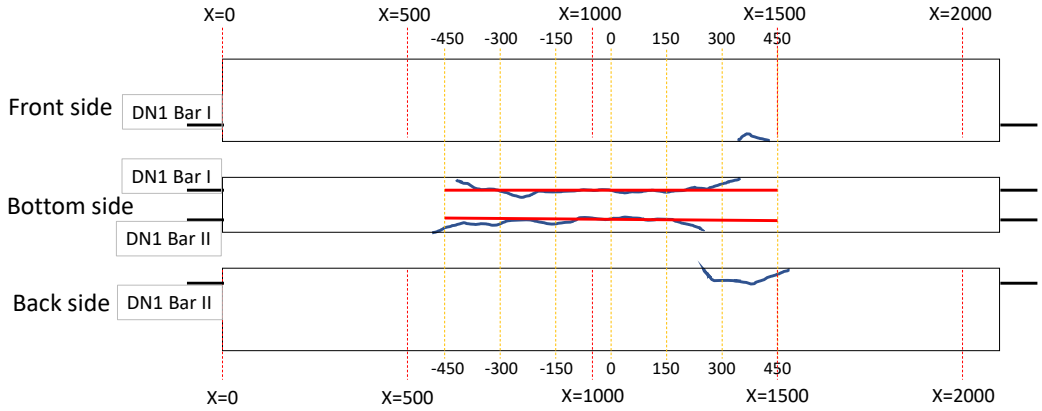

Figure B.5: Plot indicating the location of the longitudinal corrosion cracks for DN1 beam category. Horizontal red lines indicate that measured corrosion cracks were generalized to the uniform longitudinal crack in FE modelling. Here, the corrosion cracks were assumed to extend up to 80 mm from the bottom surface of the concrete beam.

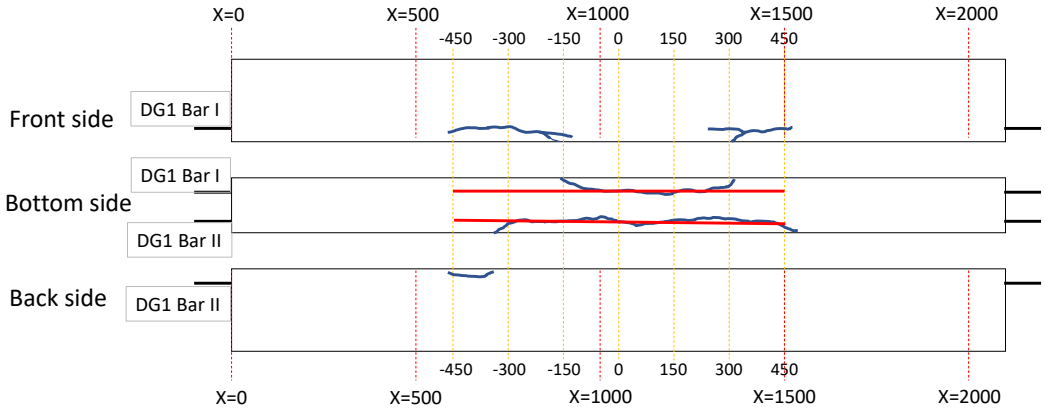

Figure B.6: Plot indicating the location of the longitudinal corrosion cracks for DG1 beam category. Horizontal red lines indicate that measured corrosion cracks were generalized to the uniform longitudinal crack in FE modelling. Here, the corrosion cracks were assumed to extend up to 78 mm from the bottom surface of the concrete beam.

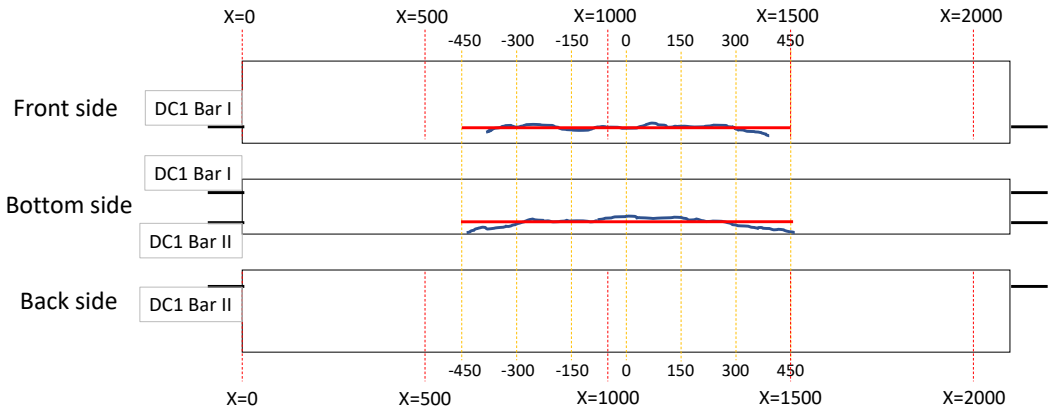

Figure B.7: Plot indicating the location of the longitudinal corrosion cracks for DC1 beam category. Horizontal red lines indicate that measured corrosion cracks were generalized to the uniform longitudinal crack in FE modelling. Here, the corrosion cracks at the location of Bar II were assumed to extend up to 76 mm along the height of the beam from bottom surface of the concrete beam. However, the corrosion cracks at the location of bar I were assumed to extend 80 mm along the width of the beam from the front side.

Table B.5: Position and crack width of corrosion-induced cracks measured by Yang [18].

x-coordinate [mm]	**crack width [mm]**	**x-coordinate [mm]**	**crack width [mm]**
DN1-bar II		**DN1-bar I**	
600	0.14	600	0.00
750	0.90	750	0.69
900	1.19	900	0.59
1050	1.21	1050	0.76
1200	1.00	1200	0.99
1350	0.66	1350	0.26
1500	0.20	1500	0.05
DG1-bar II		**DG1-bar I**	
600	0.27	600	0.03
750	1.29	750	1.26
900	1.66	900	0.98
1050	1.69	1050	1.08
1200	1.80	1200	0.67
1350	1.14	1350	0.60
1500	0.16	1500	0.09
DC1-bar II		**DC1-bar I**	
600	0.00	600	0.00
750	0.59	750	0.35
900	1.27	900	0.66
1050	1.78	1050	0.77
1200	1.49	1200	1.22
1350	0.36	1350	0.51
1500	0.22	1500	0.00

Table B.6: Resulting tensile strength and strain for the concrete elements at the location of corrosion induced cracks corresponding to beams under category DN1, DG1 and DC1.

Stress [MPa]	**Strain [-]**
0	0
0.0124	3.72E-07
0	0

Appendix C: Corrosion modelling

Figures C.1, C.2, C.3 and C.4 show the location of corrosion pits that were considered in the FE modelling, indicating the yield length evaluated from the 3D scanning plots showing the initial and corroded cross-sectional area of the tensile reinforcement rebars. Here, I and II represents numbering of the tensile reinforcements. Furthermore, Tables C.1 and C.2 show the tensile strength and modified strain for the elements corresponding to the pitted rebars in the beam categories DN1, and DC1 respectively; these were given as input in the FE modelling.

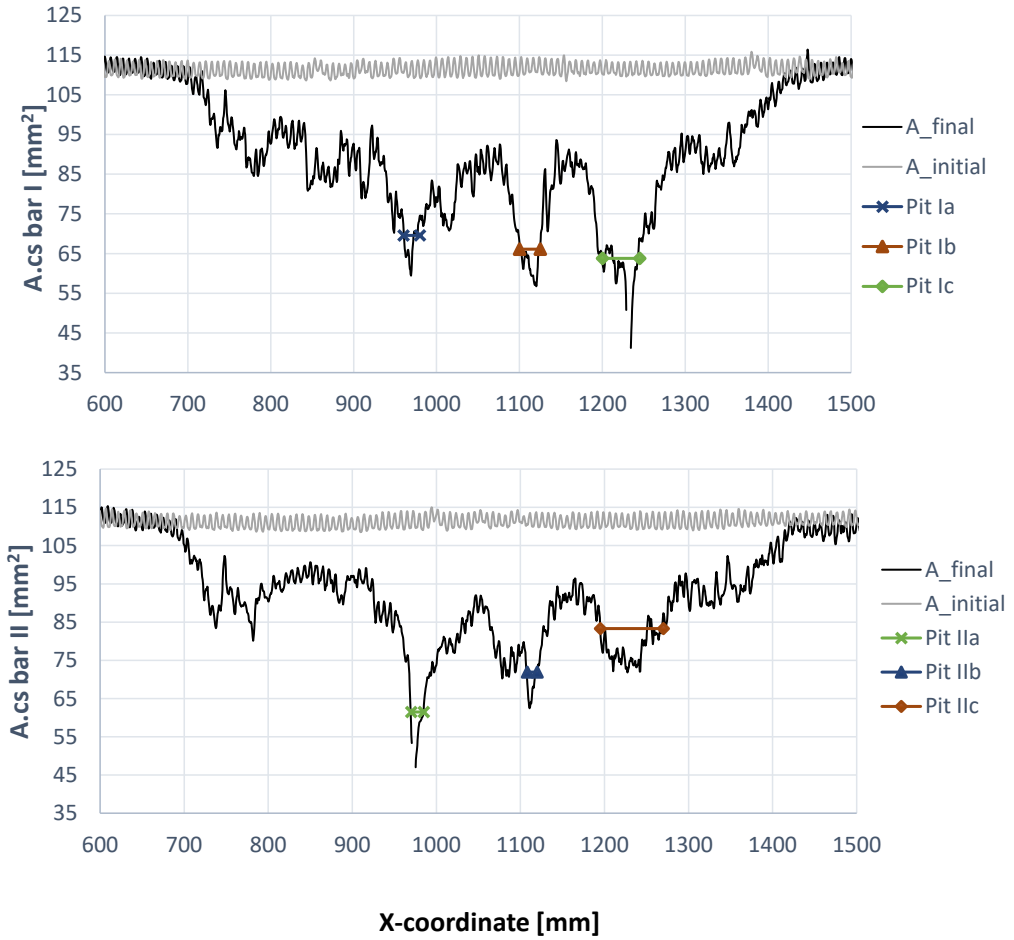

Figure C.1: Figures indicating the location of pits and yield length in 3D scanning plots, which were considered in DN1_FEA model model

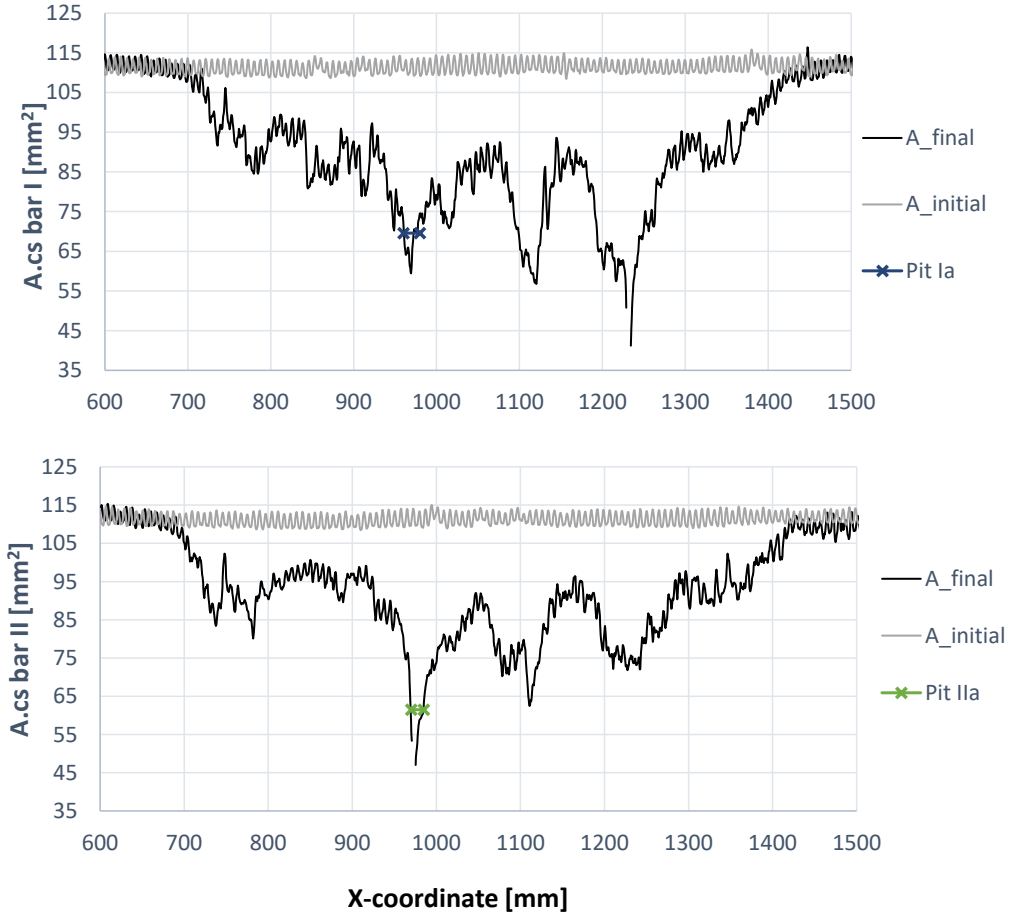

Figure C.2: Figures indicating the location of pit and yield length in 3D scanning plots, which was considered in DN1P1_FEA model. For FE model DN1P1E_FEA model, cross-sectional area of neighbouring rebar elements at both sides of pits Ia and IIa were reduced by amount of corrosion level at the end of yield penetration, μ_p, see section 5.9

Table C.1: Tensile strength and strain values for the elements corresponding to the pits in DN1 beams. Here, the strength and strain values are presented for those pits for which the ultimate and rupture strain were modified based on the yield length as described in the section 5.9. For remaining pit Ia, , tensile strength and strain inputs are shown in Table A.2. The strain corresponding to the ultimate tensile strength i.e 661 MPa was considered as ultimate strain.

DN1-pit Ib		**DN1-pit Ic**		**DN1-pit IIa**		**DN1-pit IIb**		**DN1-pit IIc**	
σ[1] [MPa]	ε_{mod}[2] [%]	σ[1] [MPa]	ε_{mod}[2] [%]	f_{sy}[1] [MPa]	ε_{mod}[2] [%]	σ[1] [MPa]	ε_{mod}[2] [%]	σ[1] [MPa]	ε_{mod}[2] [%]
0	0	0	0	0	0	0	0	0	0
530	0.298	530	0.298	530	0.298	530	0.298	530	0.298
570	0.5	570	0.5	570	0.5	570	0.5	570	0.5
605	1.5	605	1.5	605	1.5	605	1.5	605	1.5
635	2.78	635	2.78	635	2.78	635	2.78	635	2.78
661	10.1	661	9.1	661	6.1	661	4.9	661	7.6
650	15	650	13.5	650	9	650	7.2	650	11.3
0	15.01	0	13.01	0	9.01	0	7.201	0	11.301

[1] σ - tensile strength

[2] ε_{mod} - modified tensile strain for pits

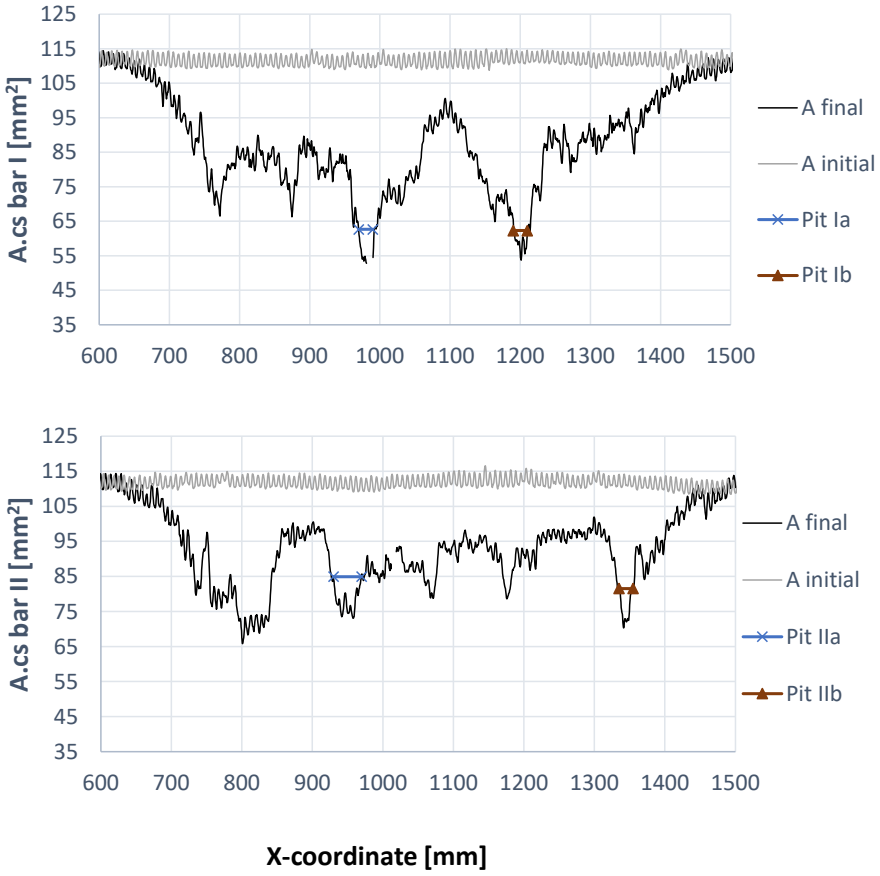

Figure C.3: Figures indicating the location of pits and yield length in 3D scanning plots, which were considered in FE modelling of DG1 beam category.

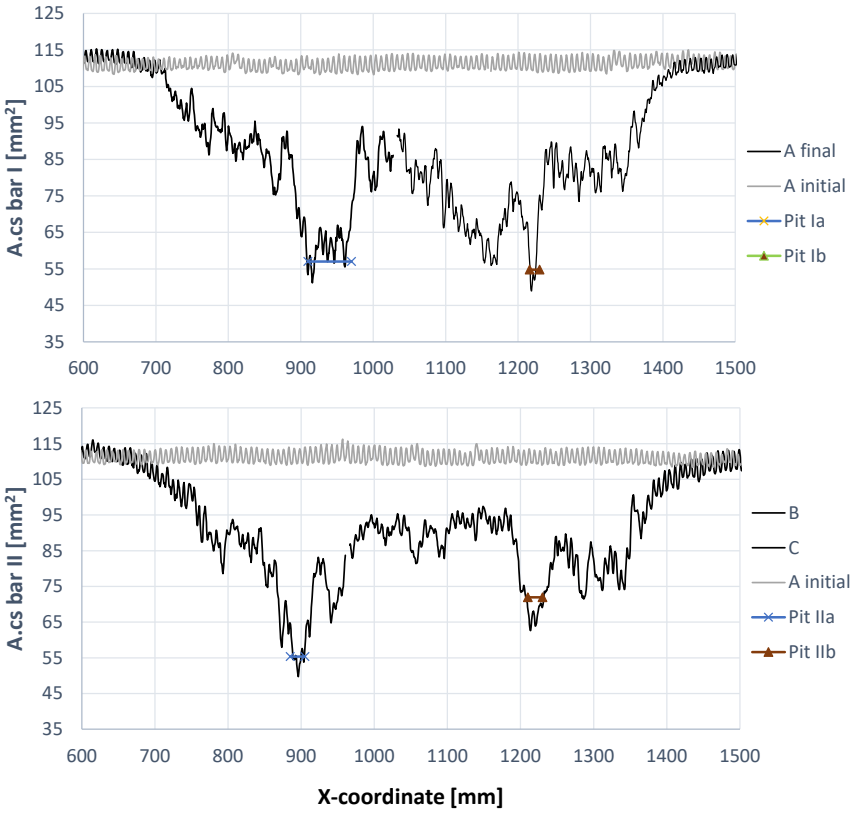

Figure C.4: Figures indicating the location of pits and yield length in 3D scanning plots, which were considered in FE modelling of DC1 beam category.

Table C.2: Tensile strength and modified strain input for a pit Ib of DC1 beam category. Here the stress and strain values are presented for a pit-Ib for which the ultimate and rupture strain was modified based on the yield length as described in the section 5.9. For all other pits (Ia, IIa and IIb), tensile strength and strain inputs are same as for bottom rebar as shown in Table A.2. The strain corresponding to the ultimate tensile strength i.e 661 MPa was considered as ultimate strain.

DC1-pit Ib	
σ[1][MPa]	ε_{mod}[2][%]
0	0
530	0.298
570	0.5
605	1.5
635	2.78
661	4.05
650	6
0	6.01

[1] σ - tensile strength
[2] ε_{mod} - modified tensile strain for pits

Appendix D: Material properties and interface properties for DG1 and DC1 beam models

In this section tensile strength and strain input for FRP materials and interface properties for modelling of strengthened beams are presented.

Table D.1: Tensile strength and strain input for FRP materials in FE modelling

GFRP sheet		CFRP plate		Inclined U-jackets		Vertical U-jackets (x-direction)		Vertical U-jackets (y-direction)	
stress [MPa]	strain [%]	stress [MPa]	strain [%]	stress [MPa]	strain [%]	stress [MPa]	strain [%]	stress [MPa]	strain [%]
367.64	1.82	2717.80	1.27	714.24	1.24	714.24	1.24	88.04	1.24

Table D.2: Non-linear interface properties in DG1 and DC1 beam model.

Bond stress(τ)[MPa]	slip(s) [mm]
GFRP sheet to concrete interface	
0	0
4.71	0.06
0	0.149
CFRP plate to concrete interface	
0	0
5.74	0.07
0	0.182
U-jackets to concrete/FRP	
0	0
5.74	0.07
0	0.182

Table D.3: Linear interface properties for U-jackets in DG1 beam model.

Linear interface properties for U-jackets	
Normal stiffness modulus (z-direction)	$3.55*10^{12}$ N/m^3
Shear stiffness modulus (x-direction)	$2.11*10^{11}$ N/m^3
Shear stiffness modulus (y-direction)	$2.11*10^{11}$ N/m^3

Appendix E: Analytical calculation for RN1 beam

Analytical calculation and validation of reference beam

Beam geometry:

$b := 150mm$ width

$h := 225mm$ height

$L := 2.1m$ total length

$L_{effective} := 1.8m$ span length

Concrete properties:

$f_{cm} := 0.8 \cdot 78.7MPa = 62.96 \cdot MPa$ cylindrical compressive strength

$f_{ctm} := 4.448MPa$ tensile strength, derived from wedge splitting test

$E_{cm} := 33.3GPa$ E-modulus

$\varepsilon_{cu2} := 0.0035$ concrete ultimate strain

Reinforcement properties:

$\phi_{bottom} := 12mm$

$\phi_{top} := 10mm$

$A_{s.bottom} := 2 \cdot \pi \cdot \frac{(\phi_{bottom})^2}{4} = 226.195 \cdot mm^2$ total bottom reinforcement area

$A_{s.top} := 2 \cdot \pi \cdot \frac{(\phi_{top})^2}{4} = 157.08 \cdot mm^2$ total top reinforcement area

$f_{sy.bottom} := 570MPa$ yield stress bottom rebars

$E_{s.bottom} := 191GPa$ E-modulus bottom rebars

$f_{sy.top} := 528MPa$ yield stress top rebars

$E_{s.top} := 200GPa$ E-modulus top rebars

$\varepsilon_{su.bottom} := 0.12$ rupture strain bottom rebars

$d_1 := 225mm - 41mm = 184 \cdot mm$ effective height bottom rebars

$d_2 := 35mm$ effective height top rebars

Assuming that reinforcement yields at strain:

$$\varepsilon_{sy.bottom} := \frac{f_{sy.bottom}}{E_{s.bottom}} = 2.984 \times 10^{-3}$$

Cracking load

Stiffness when reinforcement neglected:

$$I := \frac{b \cdot h^3}{12} = 1.424 \times 10^{-4}\,m^4$$

$$M_{cr} := f_{ctm} \cdot \left(\frac{I}{\frac{h}{2}} \right) = 5.63 \cdot kNm$$ Cracking moment

$$P_{1.cr} := \frac{M_{cr}}{\frac{L_{effective}}{2} - 300mm} = 9.382 \cdot kN$$ One point load

$$P_{tot.cr} := 2 \cdot P_{1.cr} = 18.765 \cdot kN$$ Total cracking load

Yield moment and load when yielding starts

$$\varepsilon_{cc} = \frac{\varepsilon_{sy.bottom}}{d_1 - x} \cdot (0 - x)$$ Compressive concrete strain when bottom reinforcement starts yielding

$$\varepsilon_{s.top} = \frac{\varepsilon_{sy.bottom}}{d_1 - x} \cdot \left(d_2 - x \right)$$ Top reinforcement strain when bottom reinforcement starts yielding

$$F_{sy} := f_{sy.bottom} \cdot A_{s.bottom} = 128.931 \cdot kN$$

$$F_c = \alpha_R \cdot E_{cm} \cdot \varepsilon_{cc} \cdot b \cdot x$$

$$F_{s.top} = E_{s.top} \cdot \varepsilon_{s.top} \cdot A_{s.top}$$

$$F_{sy} + F_c + F_{s.top} = 0$$ Force equillibrium

Calculate the compressive height: (assuming a triangular compressive zone)

Guess $x := 70mm$ Distance to neutral axis from top of beam

Given $f_{sy.bottom} \cdot A_{s.bottom} + \frac{1}{2} \cdot E_{cm} \cdot \left[\frac{\varepsilon_{sy.bottom}}{d_1 - x} \cdot (0 - x) \right] \cdot b \cdot x \ldots = 0$

$+ E_{s.top} \cdot \left[\frac{\varepsilon_{sy.bottom}}{d_1 - x} \cdot (d_2 - x) \right] \cdot A_{s.top}$

$x_y := \text{Find}(x) = 0.047\,m$ Compressive height

$\varepsilon_{sy.bottom} = 2.984 \times 10^{-3}$ Strain bottom reinforcement

$\varepsilon_{cc} := \frac{\varepsilon_{sy.bottom}}{d_1 - x_y} \cdot (0 - x_y) = -1.026 \times 10^{-3}$ Strain in concrete

$\varepsilon_{s.top} := \frac{\varepsilon_{sy.bottom}}{d_1 - x_y} \cdot (d_2 - x_y) = -2.633 \times 10^{-4}$ Strain in top reinforcement

$F_c := \frac{1}{2} \cdot E_{cm} \cdot \varepsilon_{cc} \cdot b \cdot x_y = -120.659 \cdot kN$

$F_{s.top} := E_{s.top} \cdot \varepsilon_{s.top} \cdot A_{s.top} = -8.272 \cdot kN$

Yielding moment:

$\beta_R := \frac{1}{3}$ Assuming a triangular compressive zone

$M_y := F_c \cdot (\beta_R \cdot x_y - d_1) + F_{s.top} \cdot (d_2 - d_1) = 21.54 \cdot kN \cdot m$ Yield moment (Moment equilibrium around bottom reinforcement)

$M_E = P_{1.y} \cdot \frac{L_{effective}}{2} - P_{1.y} \cdot 300mm$ Moment effect

$P_{1.y} := \frac{M_y}{\frac{L_{effective}}{2} - 300mm} = 35.9 \cdot kN$ One point load

$P_{tot.y} := 2 \cdot P_{1.y} = 71.801 \cdot kN$ Total yielding load

Ultimate load

$f_{su} := 621MPa$ Steel stress at calculated tensile strain of 0.0226

Rectangular stress distribution assumed (EC2-1-1 3.1.7(3))

$\lambda := 0.8$ Effective height of the compression zone

$\eta := 1.0$ Factor defining effective strength

Known:

$\varepsilon_{cc.u} := -\varepsilon_{cu2} = -0.35 \cdot \%$ Concrete crushed

Calculate the height of the compressive zone:

Assume: $x_u := 63mm$

$$x_u := root\left[f_{su} \cdot A_{s.bottom} - \eta \cdot f_{cm} \cdot \lambda \cdot x_u \cdot b - E_{s.top} \cdot \left[\frac{\varepsilon_{cc.u}}{x_u} \cdot \left(d_2 - x_u\right)\right] \cdot A_{s.top}, x_u\right]$$

$x_u = 25 \cdot mm$

Control strain of bottom bars

$$\varepsilon_{s.b.u} := \frac{\varepsilon_{cc.u}}{0 - x_u} \cdot \left(d_1 - x_u\right) = 0.0226$$

$\varepsilon_{sy.bottom} = 2.98 \times 10^{-3}$ $\varepsilon_{su.bottom} = 0.12$ i.e. yielded, not ruptured

$$\varepsilon_{s.t.u} := \frac{\varepsilon_{cc.u}}{0 - x_u} \cdot \left(d_2 - x_u\right) = 1.46 \times 10^{-3}$$ Strain in top reinforcement (In tension)

Ultimate moment:

$$M_u := \eta \cdot f_{cm} \cdot b \cdot \lambda \cdot x_u \cdot \left(x_u - \lambda \cdot x_u \cdot 0.5\right) + A_{s.top} \cdot E_{s.top} \cdot \left(\varepsilon_{s.t.u}\right) \cdot \left(d_2 - x_u\right) \ldots + A_{s.bottom} \cdot f_{su} \cdot \left(d_1 - x_u\right) = 25.6 \cdot kNm$$

$$P_{1.u} := \frac{M_u}{\frac{L_{effective}}{2} - 300mm} = 42.7 \cdot kN$$ One point load

$P_{tot.u} := 2 \cdot P_{1.u} = 85.4 \cdot kN$ Total ultimate load

Check of sectional forces

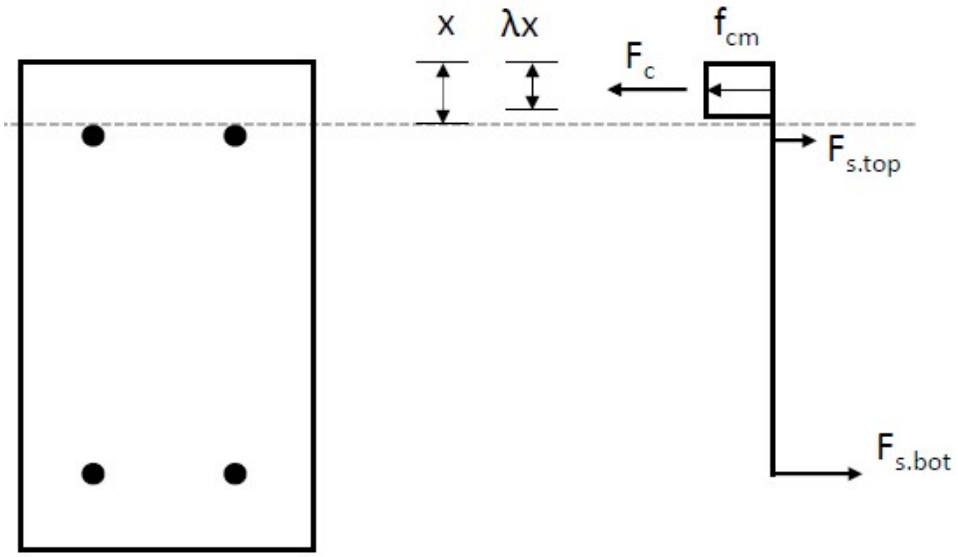

Analytical, at ultimate load 85.4kN

Bottom rebars:

$A_{s.bottom} = 226.195 \cdot mm^2$

$f_{su} = 621 \cdot MPa$

$F_{s.bot} := f_{su} \cdot A_{s.bottom} = 140.467 \cdot kN$

Top rebars:

$A_{s.top} = 157.08 \cdot mm^2$

$\varepsilon_{s.t.u} = 1.464 \times 10^{-3}$

$E_{s.top} = 200 \cdot GPa$

$F_{s.top} := E_{s.top} \cdot \varepsilon_{s.t.u} \cdot A_{s.top} = 45.986 \cdot kN$

Total tensile force in rebars:

$F_{s.tot} := F_{s.top} + F_{s.bot} = 186.453 \cdot kN$

Concrete in compression:

$b = 0.15\,m \qquad x_u = 0.025\,m$

$f_{cm} = 62.96 \cdot MPa$

$F_{cc} := \lambda \cdot b \cdot x_u \cdot f_{cm} = 186.453 \cdot kN$

FE analysis, at 85.55kN total load (Load step 499)
(Values extracted from a cracked section at x=0.91m)

Bottom rebars:

$f_{FE.s.bot} := 623.2MPa$

$F_{FE.s.bot} := f_{FE.s.bot} \cdot A_{s.bottom} = 140.965 \cdot kN$

Top rebars:

$f_{FE.s.top} := 120.7MPa$

$F_{FE.s.top} := f_{FE.s.top} \cdot A_{s.top} = 18.96 \cdot kN$

Total tensile force in rebars:

$F_{FE.s.tot} := F_{FE.s.bot} + F_{FE.s.top} = 159.924 \cdot kN$

Concrete in compression:

$x_{FE.u} := 0.0205m$

$f_{FE.c} := 57.3MPa$

$F_{FE.c} := b \cdot x_{FE.u} \cdot f_{FE.c} = 176.197 \cdot kN$

Comparison, Analytical to FE:

$$\mu_s := \frac{F_{s.tot}}{F_{FE.s.tot}} = 1.166 \qquad \mu_c := \frac{F_c}{F_{FE.c}} = 1.058$$